Improving hydroacoustic methods for monitoring suspended-sand flux and grain size in sediment-laden rivers

Jessica Marggraf, Jérôme Le Coz, Benoît Camenen, François Lauters, Guillaume Dramais, Gilles Pierrefeu, David J Topping

Received: 2 July 2024 | Revised: 5 November 2024 | Accepted: 9 December 2024

DOI: 10.1002/esp.6056

RESEARCH ARTICLE

ESPL WILEY

Improving hydroacoustic methods for monitoring suspended-sand flux and grain size in sediment-laden rivers

Jessica Marggraf[1,2] | Jérôme Le Coz[1] | Benoît Camenen[1] | François Lauters[3] | Guillaume Dramais[1] | Gilles Pierrefeu[4] | David J. Topping[5]

[1]RiverLy, INRAE, Villeurbanne, France

[2]University of Minnesota, Minneapolis, Minnesota, USA

[3]Service Etudes Eau Environnement, EDF, Saint Martin Le Vinoux, France

[4]Centre d'Essais, de Surveillance, d'Analyses et de Mesures pour l'Exploitation (CESAME), CNR, Lyon, France

[5]U.S. Geological Survey, Southwest Biological Science Center, Grand Canyon Monitoring and Research Center, Flagstaff, Arizona, USA

Correspondence
Jessica Marggraf, St. Anthony Falls Laboratory, University of Minnesota, Minneapolis, Minnesota, USA.
Email: jmarggra@umn.edu

Funding information
INRAE; CNR; EDF

Abstract

Suspended-sand concentration and grain-size data in rivers provide valuable information on the catchment's dynamics for scientists and river managers. Producing continuous measurements of suspended-sand concentrations remains a scientific challenge due to their high spatial and temporal variability. Traditional methods such as sediment-rating curves may be highly uncertain, and optical turbidity is insensitive to coarse particles when there are many fine particles. Surrogate hydroacoustic methods aim to improve sand concentration measurements. These single- or dual-frequency acoustic methods use acoustic attenuation and/or backscatter to estimate fine-sediment (i.e., silt and clay) and/or sand concentration and possibly grain size. New methods have recently been developed and applied in rivers exhibiting a wide range of sediment conditions in North America but not independently tested elsewhere by other researchers. In this article, we apply, adapt and evaluate hydroacoustic methods to continuously estimate suspended-sand concentration and grain size in an Alpine river with high suspended-sediment concentrations. From the example of the River Isère at Grenoble Campus, France, we show that the hydroacoustic methods adapted to local conditions may yield valuable sand concentration estimates consistent with traditional measurements. Compared with prior knowledge, limited additional information on the grain size can be obtained due to high uncertainties. Hydroacoustic concentration estimates are more sensitive to real changes in concentration at the event scale than traditional rating-curve methods that relate concentration to discharge only. These findings open the perspective for facilitated sand concentration monitoring at a higher temporal resolution with decreased field work.

KEYWORDS
concentration, grain size, hydroacoustics, HADCP, suspended sand

1 | INTRODUCTION

Suspended-sand concentration and grain-size data are crucial for understanding the dynamics of a river and its catchment. In highly engineered rivers, where the stream flow is regulated by dams and dikes, sand accumulation is a major issue for river management by increasing flood risk, decreasing the hydropower plant efficiency and hindering navigation (Schleiss et al., 2010, 2016; Wisser et al., 2013). Although information on sand fluxes is crucial for scientists and river managers, their measurement remains a scientific challenge. Sand suspensions are characterized by considerable spatial and temporal heterogeneity throughout the cross-section, complicating concentration and grain-size measurements. Traditionally, multiple physical samples are taken at different locations throughout the cross-section to obtain spatially distributed information and to determine cross-sectional averages (Edwards & Glysson, 1999; Hicks & Gomez, 2016; ISO 4363, 2002).

Rating-curve or transport-capacity approaches are used to determine annual suspended-sand fluxes based on frequent physical samplings (Asselman, 2000; Campbell & Bauder, 1940; Darby et al., 2015). Rating-curve methods relate sediment fluxes with discharge by fitting an empirical or a transport-capacity-based relation. Frequently applied empirical power rating curves may be corrected by introducing a critical discharge, below which no sediment transport is assumed to occur (Camenen et al., 2014; van Rijn, 1984). These methods are used to establish sediment-flux budgets, but they may be affected by large uncertainty (Cohn et al., 1989; Grasso & Jakob, 2003; Topping et al., 2021; Walling, 1977).

During the last few decades, hydroacoustic methods have been developed to improve the temporal and spatial resolution of suspended-sediment-flux measurements. These surrogate methods based on sonar technology use the attenuation of the acoustic signal and its backscattered intensity to resolve for sediment concentration (Thorne & Hurther, 2014) or sediment concentration and grain size (Topping & Wright, 2016). Initially developed in marine contexts with relatively low fine-sediment (i.e., silt and clay) concentrations (Hay, 1983; Moate et al., 2016; Thorne et al., 1993; Thorne & Hardcastle, 1997), this solid-particle theory is now increasingly used in cohesive and fluvial environments with bimodal silt–sand suspensions and non-spherical particles (Aleixo et al., 2020; Haught et al., 2017; Marrugo-Negrete et al., 2023; Venditti et al., 2016; Vergne et al., 2020). The difference between the suspensions encountered in marine and fluvial contexts, however, challenges its application in fluvial environments (Vergne et al., 2023).

In rivers, the acoustic instruments may be deployed vertically (e.g., Szupiany et al., 2019; Wood et al., 2019) or horizontally (e.g., Landers et al., 2016; Moore et al., 2013) using specifically developed instruments such as acoustic backscatter systems (ABS) or (horizontal) acoustic Doppler current profilers ((H)ADCPs) primarily used for velocity and discharge measurement. Fixed on the river bank, the HADCPs ensonify a distinct zone of the cross-section and are used to establish continuous time series of sediment (fine sediment and/or sand) concentration and possibly grain size in the cross-section (Haught & Venditti, 2023; Moore et al., 2013; Topping & Wright, 2016). Shallowness can be an issue both for vertical deployment due to blanking and for horizontal deployment due to reflections from the surface and bottom boundaries. Existing methods notably differ in the number of frequencies used (commonly one or two) and the performed calibrations. Although based on acoustic theory, most hydroacoustic methods are semi-empirical, because they rely on suspended-sediment measurements for calibration. In recent works, this dependence on *in situ* samples has been reduced (Moore et al., 2012; Moore et al., 2013; Topping & Wright, 2016; Vergne et al., 2020).

One of the most validated methods with datasets at multiple operational monitoring sites and large sand concentrations is the dual-frequency method of Topping and Wright (2016). Like other recent studies (Hanes, 2012; Moore et al., 2013), it utilizes theory to relate fine-sediment concentration to attenuation and, after correcting for the backscatter from fine sediment, sand concentration to backscatter. This method estimates the fine-sediment and sand concentrations and sand grain size in the entire cross-section by using the acoustic response in the ensonified volume as a proxy. Developed in the fine-sand-dominated River Colorado and Rio Grande, this method has been applied to the River Chippewa (Dean et al., 2022), which is dominated by coarser sand grain sizes, but has almost no silt and clay in suspension. Consequently, the Topping and Wright (2016) method had only limited testing in fluvial environments with coarser sand grain sizes and high suspended fine-sediment concentrations. Reproducing and testing the method of Topping and Wright (2016) under different conditions is needed to obtain valuable information on the performance of this specific method and allow for conclusions on the use of acoustic methods for determining river suspensions in general.

The aim of this article is to evaluate traditional and hydroacoustic methods to estimate suspended-sand concentration and grain size continuously on the example of the River Isère, France, at Grenoble Campus. The advantages of the chosen study site are the bimodal, highly concentrated suspension with considerable proportion of sand and the existence of a long-term hydro-sedimentary measurement station. The dual-frequency acoustic method developed by Topping and Wright (2016) was applied, adapted and evaluated using acoustic measurements obtained by 400 kHz and 1 MHz HADCPs and numerous concurrent suspended-sediment measurements performed from April 2021 to June 2023. The acoustic methods were evaluated by comparing (1) the acoustic sand concentration and grain-size estimates with concurrent samplings and (2) the modelled and measured attenuation and backscatter.

2 | DATA

2.1 | Study site: River Isère

The traditional and hydroacoustic methods for sand concentration estimation are evaluated on the example of the hydro-sedimentary station of the River Isère at Grenoble Campus (5.768936°, 45.197504°) in the French Alps (Figure 1). The advantages of this study site are the existence of a long-term hydro-sedimentary station measuring discharge and total suspended-sediment concentration C_{tot} every 30 min (Figure 2; Thollet et al., 2021), as well as a wide range in sand concentration, and varying ratios between the fine-sediment and sand concentrations. The total suspended-sediment concentration is measured using optical turbidity, which is calibrated with frequent total suspended-sediment concentrations obtained by filtration on samples taken by an ISCO automatic pumping sampler.

The River Isère, whose bed is composed of gravel and sand, is a major tributary of the River Rhône (Table 1). It has a complex alpine catchment composed of high mountain areas and lowlands (Antoine et al., 2020; Dumas, 2007; Némery et al., 2013). At the interface of the mountains and the lowlands, the Grenoble Campus hydro-sedimentary station is located. The catchment (5720 km^2) is strongly impacted by human activities, for example, dikes and dams for flood protection and hydraulic energy production (Némery et al., 2013; Thollet et al., 2021), where regular dam flushes are conducted.

2.2 | Suspended-sediment data

Three different suspended-sediment datasets are available at the study site at Grenoble Campus: (1) suspended-sediment

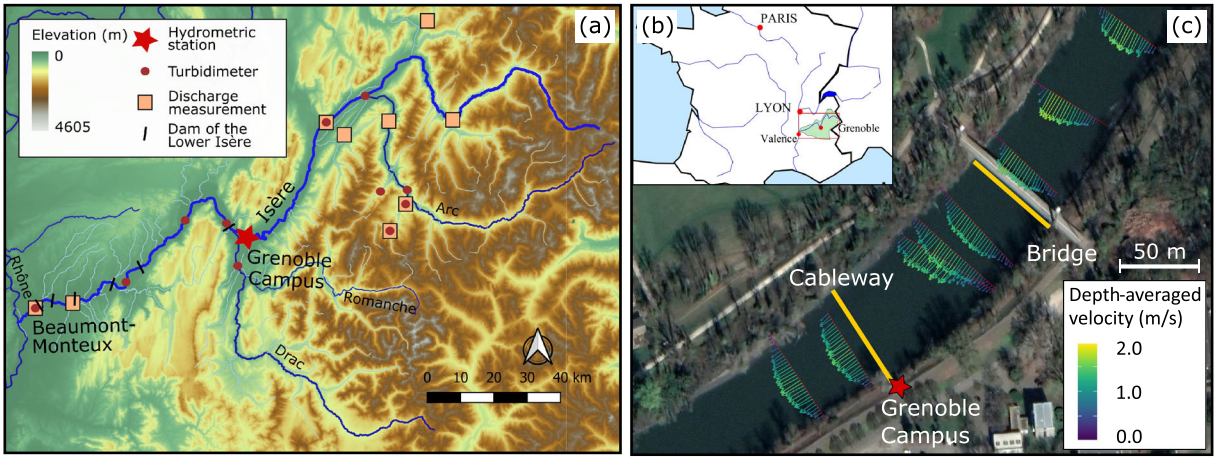

FIGURE 1 The River Isère at the Grenoble Campus study site: (a) location in the River Isère catchment (elevation data: RGE ALTI(R), 2021), (b) location of the catchment map France, (c) aerial photograph of the river reach with the bridge and cableway sampling cross-sections and depth-averaged velocities measured using an ADCP for discharge $Q = 287\ m^3/s$ (data processed using QRevInt software; Lennermark & Hauet, 2022).

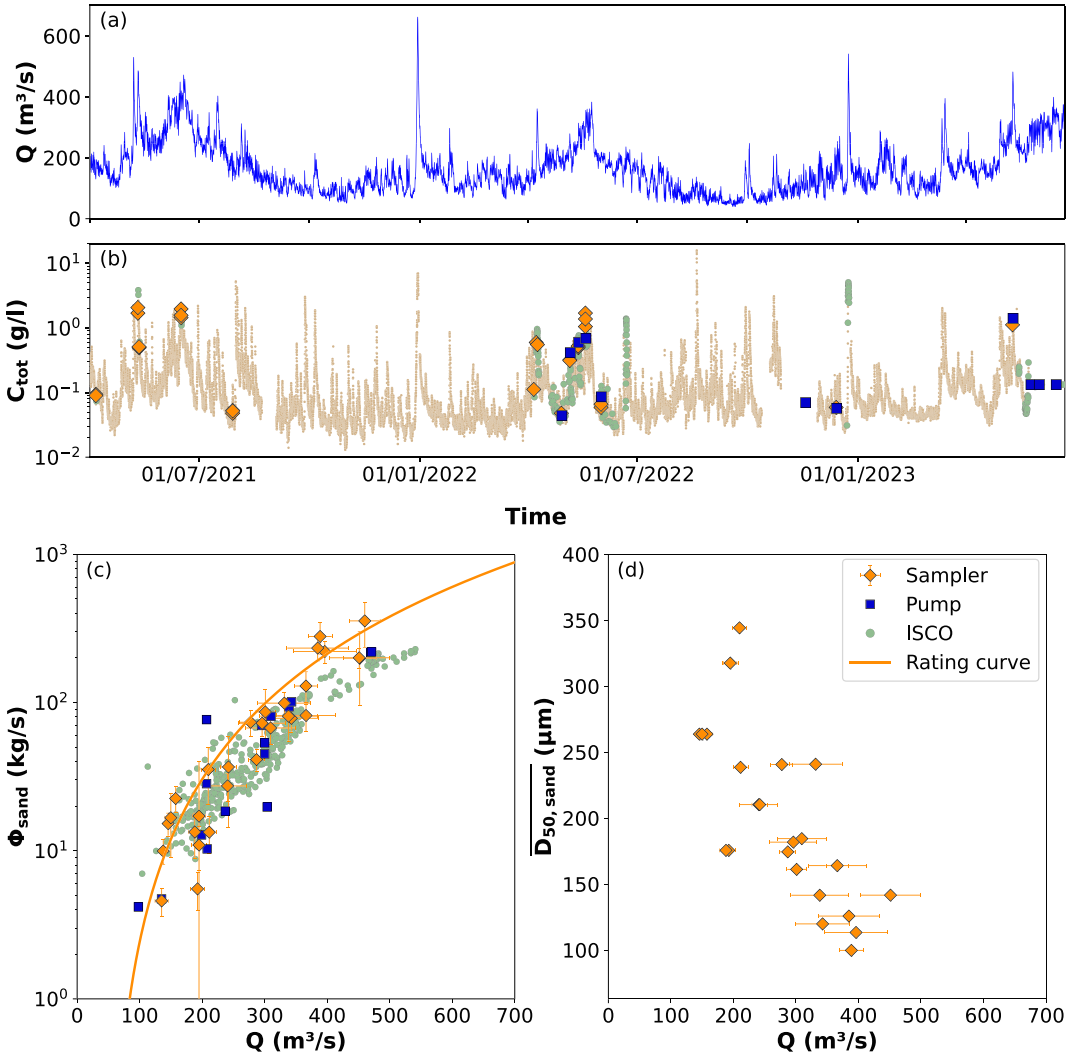

FIGURE 2 Data collected at the hydro-sedimentary station of Grenoble Campus in the River Isère: (a) Discharge Q and (b) total suspended-sediment concentration C_{tot} and dates of concurrent suspended-sediment measurements from 1 April 2021 to 22 June 2023 (Thollet et al., 2021), (c) empirical sediment-rating curve (Equation 1) calibrated using the sampler suspended-sediment measurements only (obtained using US P-72, US P-6 and Delft bottle samplers and analysed as described by Marggraf et al., 2024) and (d) averaged cross-sectional sand median grain size $\overline{D_{50,sand}}$ determined using the sampler suspended-sediment measurements only.

measurements made using different isokinetic samplers, (2) suspended-sediment measurements made using a pump PP36 and (3) calibrated ISCO automatic pump data.

2.2.1 | Sampler: Mean cross-sectional fine-sediment and sand concentrations

The sampler suspended-sediment measurements consist of 31 measurements performed at the cableway and bridge cross-sections in the River Isère at Grenoble Campus yielding velocity-weighted mean cross-sectional fine-sediment and sand concentrations (see Section S1.1 in the Supporting Information for details). Point samples were collected at different locations throughout the river cross-section using specific suspended-sediment samplers, the US P-6 (manufactured by Carnet Technology, USA), US P-72 (manufactured by Performance Results Plus Inc., USA) and the Delft bottle (manufactured by Royal Eijkelkamp, The Netherlands) (FISP, 1941). At the cableway cross-section, the US P-6 and US P-72 samplers were deployed and sampled typically five to seven verticals with four or five points each (Figure 3a). The five verticals closest to the left bank intersect the volume ensonified by the HADCPs; one sample along each of those verticals was collected within the ensonified volume. At the bridge cross-section, the Delft bottle sampler was exposed at five verticals with four to five sampling points each (Figure 3b). Sand concentrations of US P-6 and US P-72 samplers were determined by filtration, sand fluxes obtained by the Delft bottle sampler were converted to concentrations using velocity measurements.

TABLE 1 Hydraulic and sedimentary properties of the River Isère at Grenoble Campus. Measurements of bed slope are performed at the station Isère-Pont du tram, located 1270 m downstream and vary between 0.2% and 0.6% during the study period (Thollet et al., 2021).

Parameters	Value
Annual mean discharge (m^3/s)	178
Width at mean discharge (m)	~ 70
Two-year flood peak discharge (m^3/s)	600
Bed slope (%)	~ 0.35

Mean cross-sectional suspended-sand concentrations for each measurement were determined following the sand discharge computing (*SDC*) method (Marggraf et al., 2024). This method combines point sand concentrations with simultaneous velocity and discharge measurements obtained using multitransect ADCP measurements using Teledyne RDI RioGrande, StreamPro and Sontek M9 instruments. Point sand concentrations are interpolated and extrapolated vertically using the vertical concentration profile of Camenen and Larson (2008) and laterally using the depth as a proxy for bed shear stress. As both sand concentration and flow velocity are interpolated on the same regular grid covering the entire cross-section, calculations of spatially distributed sand flux, querying sand concentration in designated areas and determinations of mean cross-sectional sand concentration are possible.

Mean cross-sectional sand concentrations determined using the Delft bottle and the corresponding measurement protocol were corrected by a factor of 2.37 to avoid the observed bias compared with the US P-6 and comparable pump PP36 samples (Marggraf, 2024). The mean cross-sectional fine-sediment

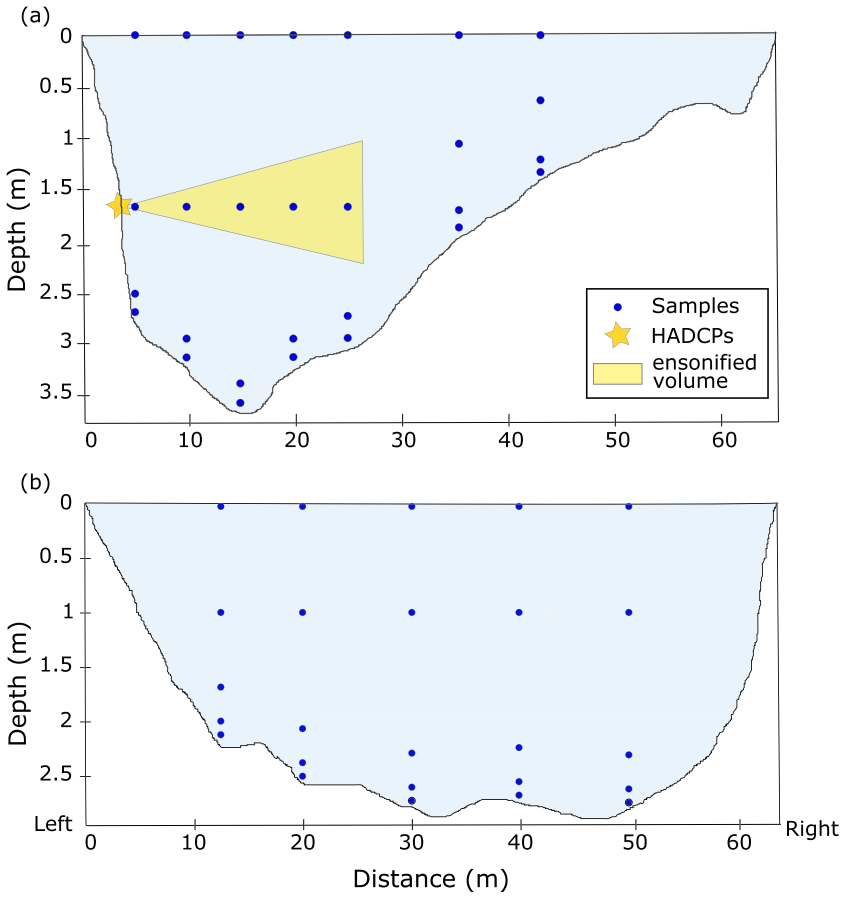

FIGURE 3 (a) Cableway and (b) bridge measurement cross-sections in the River Isère at Grenoble Campus with the zone ensonified by the 1 MHz HADCP and sampling points for sampler suspended-sediment measurements using US P-72 or US P-6 samplers (modified from Marggraf et al. (2024)).

TABLE 2 Average, velocity-weighted properties of the sand and fine-sediment suspensions: median grain size $\overline{D_{50}}$, standard deviation of the grain-size distribution σ and reference sand concentration (Section 3.4). 'Measured' values are the average of the laboratory-analysed sampler suspended-sediment measurements, and 'calibrated' values correspond to the results of the *in situ* acoustic calibration of the reference suspension described in Section 3.4.

Parameters	Measured	Calibrated
$\overline{D_{50,\,\mathrm{sand}}}$	195 μ m	200 μ m (151–264 μ m)
σ_{sand}	0.59 ϕ	0.59 ϕ
$\overline{C_{\mathrm{sand,\,ref}}}$		0.2 g/L
$\overline{D_{50,\,\mathrm{fines}}}$	14 μ m	1 μ m
σ_{fines}	2.37 ϕ	1.4 ϕ

concentration is the arithmetic mean of all point fine-sediment concentrations determined using the US P-6 and US P-72 samplers due to their relative homogeneity throughout the cross-section (Marggraf, 2024). These sampler suspended-sediment measurements yield the average suspension properties during the measurement period from April 2021 to June 2023 (Table 2).

2.2.2 | Pump PP36: Mean cross-sectional sand concentrations

The second dataset contains 16 mean cross-sectional sand concentrations determined using the pump PP36 manufactured by SDEC France. Sand concentrations were obtained using the sample's dry mass and the pumped volume. The vertical integration is based on exponential laws empirically fitted to the measured point concentrations, while the lateral integration applies a linear regression. Seven of these measurements were performed simultaneously with previously described sampler suspended-sediment measurements. During all measurements, the pump PP36 was installed on the frame of the Delft bottle. When using both samplers simultaneously, the pump PP36 was fixed at the same height as the Delft bottle's nozzle. Due to resulting temporal overlap, this dataset is not completely independent from the sampler suspended-sediment measurements although the samplings themselves are independent.

2.2.3 | ISCO automatic pump: Point concentrations at the river bank

The third dataset is composed of 403 ISCO automatic pump samples taken at the hydro-sedimentary station at Grenoble Campus on the left riverbank during the previously described measurements and additional periods. All ISCO sand concentration results $C_{\mathrm{sand,\,ISCO}}$ determined by filtration are calibrated to be representative for the cross-section: $C_{\mathrm{sand,\,ISCO,\,corr}} = 0.36 \times C_{\mathrm{sand,\,ISCO}}^{0.27}$ (Marggraf, 2024), following the index-concentration method (Camenen et al., 2023; Santini et al., 2019). This correction was determined by relating the sand concentration obtained by ISCO point samples with mean cross-sectional sand concentrations obtained by simultaneous suspended-sediment samplings. It may introduce a bias for very low and very high concentrations due to the calibration with a limited number of such extreme concentrations (Figure 2c). Although this dataset is affected by a higher uncertainty than that of the two previous ones, its advantage is its relatively high temporal resolution during flood events or dam flushes.

2.2.4 | Grain-size measurements

Grain-size measurements were made using a Malvern Mastersizer 3000 laser-diffraction instrument. Prior to the grain-size analysis, the fine-sediment and sand fractions were separated by sieving using a 63 μ m sieve. The most appropriate measurement protocol was determined as described by Laible et al. (2023) and Marggraf (2024), after comparing the instrument's results to the traditional sieving method and to three other laser-diffraction instruments. Ultrasound and a stirrer speed of 2500 RPM were used to destroy aggregates and to measure primary particles only, however, differences between *in situ* and *ex situ* grain sizes of the fine-sediment fraction are possible (de Lange et al., 2024).

Although laser-diffraction measurements have been shown to yield grain-size distributions of fine sediment that are much coarser than other laboratory methods (Beuselinck et al., 1998; Konert & Vanderberghe, 1997; Kun et al., 2013), all measurements were made using the laser-diffraction method. Velocity-weighted mean cross-sectional grain sizes were determined by averaging the available grain-size measurements for each sampler suspended-sediment measurement following the ISO 4363 (2002) approach.

As can be seen in Figure 2d, we observed a decreasing median sand grain-size from 300 μ m for low discharges ($Q \approx 200\,\mathrm{m^3/s}$) to 125 μ m for high discharges ($Q \approx 400\,\mathrm{m^3/s}$). It could be explained by an activation of finer sand sediment sources during high discharges, for example, bank or flood deposits, leading to finer sand grain sizes.

2.3 | Application of the rating-curve approach

For comparison with the acoustic methods, an empirical power rating curve using a critical discharge threshold (Camenen et al., 2014; van Rijn, 1984) is applied to continuously determine the sand flux Φ_{rc}:

$$\Phi_{\mathrm{rc}} = a(Q - Q_{\mathrm{cr}})^b, \tag{1}$$

where a and b are equation parameters and Q is the discharge measured at the hydro-sedimentary station. This rating curve is fitted to the sand flux through the entire cross-section determined by the sampler suspended-sediment measurements (Figure 2c). The best fit ($R^2 \approx 0.81$) is obtained using the following parameters: critical discharge $Q_{\mathrm{cr}} = 50\,\mathrm{m^3/s}$, $a = 0.0003$ and $b = 2.3$. The observed scatter may be caused by natural and anthropological influences upstream of Grenoble, for example, affecting the grain size and the sediment supply. At high discharges, the ISCO samples underestimate the sand flux compared with the sampler and pump PP36 measurements, which may be caused by a bias in the ISCO calibration (Section 2.2.3).

2.4 | Verification of the application conditions

Prior to the application of the method of Topping and Wright (2016), we verify that the two main application conditions are met at our

study site in the River Isère at Grenoble Campus. Those requirements are (1) the relations of the average sand and fine-sediment concentrations in the cross-section with those in the ensonified volume are relatively stable under all occurring conditions (i.e., variations in these relations are small and random), and (2) the suspension is relatively homogeneous in the ensonified volume. While the first requirement has to be met to successfully apply the method, the second condition allows for more precise sand concentration and grain-size estimates.

First, we verify the relations of the average sand and fine-sediment concentrations in the cross-section with those in the ensonified volume. Both relations are strong ($R^2 > 0.93$), and no discharge- or concentration-dependent shifts are visible (Figure 4a,b). Consequently, as this major requirement is met, the method of Topping and Wright (2016) can be applied to our study site.

Second, the relatively homogeneous distribution of concentration along the acoustic beam is verified using the concentrations interpolated on a regular grid by the *SDC* method. Therefore, concentrations are extracted along the acoustic beam for all sampler suspended-sediment measurements made at the cableway cross-section. As expected, fine-sediment concentrations are relatively homogeneously distributed along the acoustic beams (Figure 4d). In contrast, sand concentrations vary with a factor of two along the beams, which is still acceptable (Figure 4c).

2.5 | Acoustic measurements

Two HADCPs, a 400 kHz AWAC and a 1 MHz AquaDopp manufactured by Nortek, were used for the acoustic measurements in the River Isère at Grenoble Campus following a similar measurement protocol to that of Topping and Wright (2016) noted in their Table 1. These instruments were installed in March 2021 at the hydro-sedimentary station at Grenoble Campus approximately 2 m higher than the deepest point of the cross-section (Figure 3 and Section S1.2 in the Supporting Information for details) to measure as close to the bed as possible, however, avoiding reflection from the bed. The two HADCPs come with monostatic transducers and a temperature sensor and were connected to the power grid. Acoustic measurements were made every 10 min, and background noise measurements were made via passive measurements (Table 3; for more details, see Marggraf, 2024).

3 | METHODS

3.1 | Data preprocessing

ADCPs typically register the raw acoustic signal amplitude *A* (counts), the pressure and the water temperature. Topping and Wright (2016,

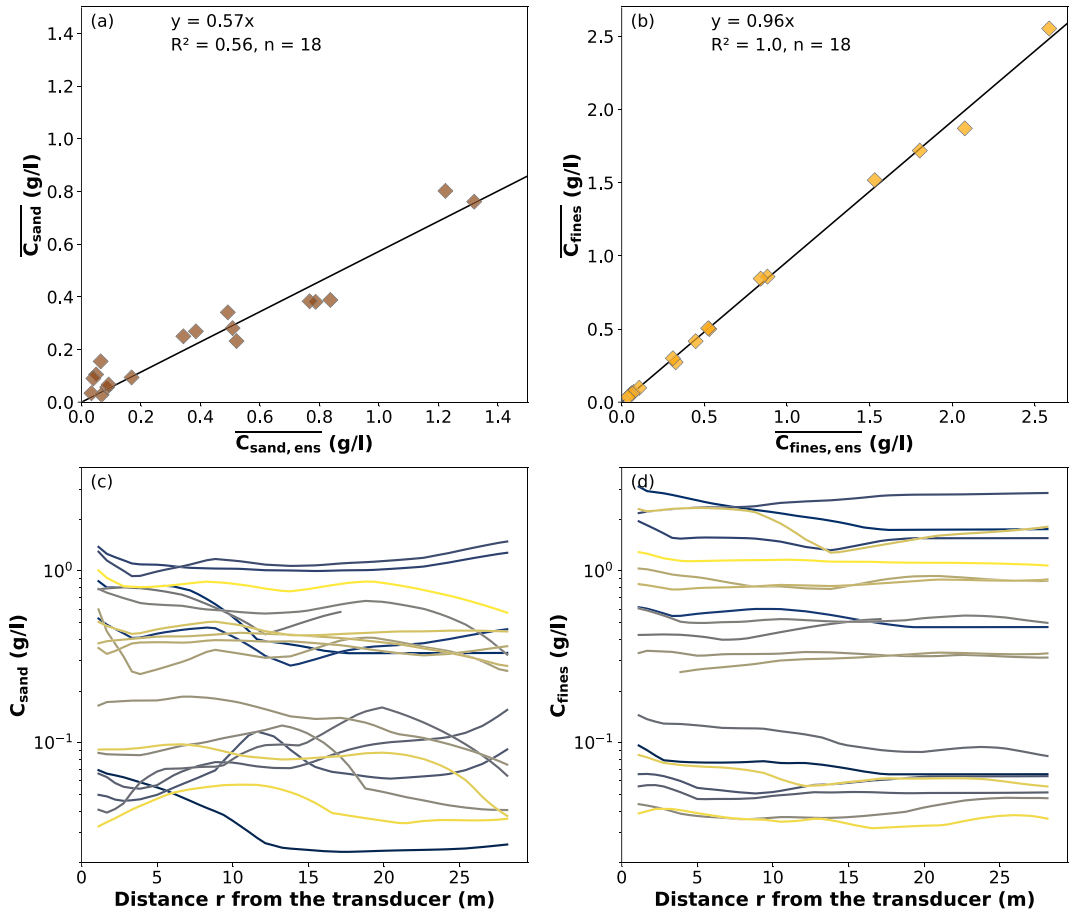

FIGURE 4 Verification of the application conditions: relations of the mean cross-sectional suspended (a) sand $\overline{C}_{sand}$ and (b) fine-sediment $\overline{C}_{fines}$ concentrations with the suspended-sand $\overline{C}_{sand, ens}$ and fine-sediment $\overline{C}_{fines, ens}$ concentrations, respectively, averaged in the valid cells along the beam, and suspended (c) sand and (d) fine-sediment concentrations extracted from the regular grid obtained by the *SDC* method along the acoustic beam in the River Isère at Grenoble Campus during the sampler suspended-sediment measurements at the cableway cross-section (modified from Marggraf, 2024).

TABLE 3 Measurement protocol used for the 400 kHz AWAC and 1 MHz AquaDopp HADCP in the River Isère at Grenoble Campus.

Parameters	400 kHz	1 MHz
Number of cells	50	64
Cell size (m)	0.5	0.4
Blanking distance (m)	0.92	0.18
Profile interval (s)	600	600
Averaging interval (s)	300	300
Ping rate (Hz)	0.75	2
Power level	Low+	Low+
Measurement load (%)	67	58
Radius of the transducer (m)	0.1	0.025
Downing critical distance (m)	8.4	1.3

p. 15 and Appendix 7) consider the measurement in a cell as valid and include it into the following acoustic analysis if the acoustic amplitude A is higher than the effective-noise floor A_E. This effective-noise floor is the sum of the instrument-noise floor determined by passive acoustic measurements and the iteratively guessed noise floor offset A_{offset}. The latter is used to remove the part of the acoustic beam where the amplitude tends to asymptotically approach the instrument-noise floor in a curved manner.

Using the distance r of the cell centre from the transducer, Topping and Wright (2016, eq. 24) calculate the fluid-corrected backscatter B_F in all valid cells as

$$B_F = b_{SF}A + 20\log_{10}(\psi r) + 2\alpha_w r, \quad (2)$$

where b_{SF} (dB/count) is a scale factor, ψ is the near-field correction (Downing et al., 1995) set equal to 1 in this study, because no measurements are made in the near field, and α_w (dB/m) is the coefficient of absorption for acoustic energy in water calculated using the formula of Schulkin and Marsh (1962).

The acoustic attenuation due to sediments α_{sed} (dB/m) is defined using the slope of a least-squares linear regression fitted on all valid values of the fluid-corrected backscatter B_F on the distance from the transducer r divided by -2 assuming that the suspension is homogeneous along the acoustic beam (Section 2.4). The more the suspension is homogeneous in the ensonified volume, the more the profile will be linear and the uncertainty in the determination of α_{sed} will decrease.

Using α_{sed} and the fluid-corrected backscatter B_F, the relative backscatter B is defined as in Topping and Wright (2016, eq. 25):

$$B = 2\alpha_{sed}r + B_F. \quad (3)$$

The beam-averaged backscatter $\overline{B}$ (dB) is the average of the relative backscatter B in all valid cells.

3.2 | Single-frequency calibration procedure (SFCP)

The SFCP is the first step of the dual-frequency method and described by Topping and Wright (2016) in their Appendix 7. SFCP is performed separately for each of the two frequencies used at the study site. It uses the attenuation and beam-averaged backscatter measurements and the suspended fine-sediment and sand concentrations to estimate single-frequency sand concentrations averaged over the entire cross-section (Figure 5). The procedure is based on a separation of the grain-size fractions, assuming that attenuation is mostly caused by fine sediments and that backscatter is mostly caused by sands. To avoid inclusion of conditions where backscatter is mostly from the fine sediment and not from the sand, samples with high fine-sediment to sand concentration ratios are not used in the SFCP.

The acoustic response of a suspension depends on the concentration and the grain size, so that a bimodal suspension is described by four unknowns: the concentrations and median grain sizes of the fine-sediment and sand fractions, respectively. A single-frequency approach yields only two parameters (attenuation and backscatter); thus, it cannot fully describe a bimodal suspension in terms of concentration and grain size. Therefore, the grain sizes of the sand and fine-sediment fractions are each fixed using a reference grain size (see Section 3.4 for details). In the SFCP, changing grain sizes are not detected as grain size changes but as concentration changes. This leads to a grain-size bias in the SFCP's results, the correction of this bias is the aim of the dual-frequency *RUTS*-based approach (Section 3.3; Topping & Wright, 2016, Appendix 8).

3.2.1 | Determination of the mean cross-sectional suspended fine-sediment concentration

The fine-sediment (i.e., silt and clay) concentration averaged over the entire cross-section is estimated for each frequency i relating the fine-sediment concentrations $\overline{C_{fines,i}}$ to simultaneous attenuation measurements $\alpha_{sed,i}$ (Topping & Wright, 2016, pp. 17–19). We convert here the notation used by Topping and Wright (2016) to the more widely used form including the sediment-attenuation constant:

$$\overline{C_{fines,i}} = \frac{1}{\zeta_{fines,i}}\alpha_{sed,i}, \quad (4)$$

where $\zeta_{fines,i}$ ((dB L)/(m mg)) is the sediment-attenuation constant determined for the fine-sediment reference suspension (see Section 3.4):

$$\zeta_{fines,i} = \zeta_{s,fines,i} + \zeta_{v,fines,i}, \quad (5)$$

where $\zeta_{s,fines,i}$ is the scattering attenuation and $\zeta_{v,fines,i}$ is related to the viscous attenuation integrated over the entire fine-sediment reference distribution as introduced by Moore et al. (2013) using the normalized total scattering cross-section χ_s (Moate & Thorne, 2012) and the normalized total viscous cross-section χ_v (Urick, 1948).

This step is performed for both frequencies, and the average of the two single-frequency estimates for every time step yields the acoustically estimated mean cross-sectional suspended fine-sediment concentration $\overline{C_{fines,HADCP}}$. These calibrations can be found in Section S2.1 in the Supporting Information.

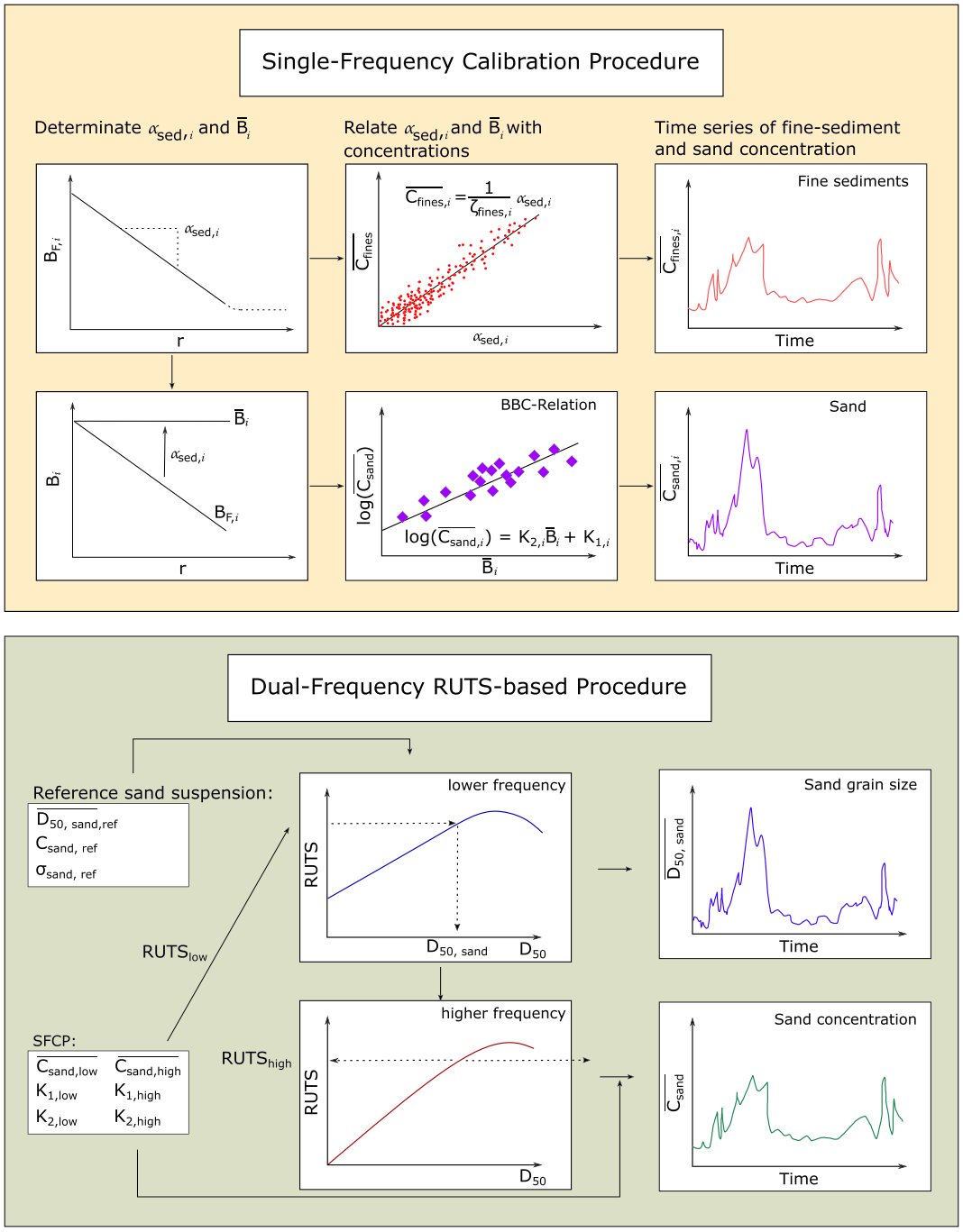

FIGURE 5 Schematic workflow of the Topping and Wright (2016) dual-frequency method composed of the single-frequency calibration procedure (SFCP) and the dual-frequency *RUTS*-based procedure. See text for the definitions of the variables.

3.2.2 | Determination of the single-frequency mean cross-sectional suspended-sand concentration

The single-frequency sand concentration $\overline{C_{sand,\,i}}$ averaged over the entire cross-section for each frequency i is defined using the beam-averaged backscatter $\overline{B_i}$ (Figure 5):

$$\overline{C_{sand,\,i}} = 10^{K_{1,i}+K_{2,i}\,\overline{B_i}}, \tag{6}$$

where $K_{1,i}$ and $K_{2,i}$ are the intercept and slope of the base-backscatter calibration (*BBC*) defined by Topping and Wright (2016, eq. 60):

$$\log_{10}(\overline{C_{sand,\,sampler}}) = K_{2,i}\,\overline{B_{base,i}} + K_{1,i}. \tag{7}$$

This *BBC* relation is established using only the suspended-sediment measurements satisfying two requirements: (1) The ratio $S = \overline{C_{fines}}/\overline{C_{sand}}$ between the fine-sediment and sand concentrations is small, ideally <2, and (2) the median sand grain-size range is small, ideally $0.25\,\phi$ of the reference sand median grain size $\overline{D_{50,\,sand,\,ref}}$ (Topping & Wright, 2016, p. 31). The latter is the sand median grain size that describes best the widest range of possible grain-size variation at the study site (see Section 3.4 for its definition and estimation). The beam-averaged backscatter measured during these suspended-sediment measurements included into the *BBC* relation is the base backscatter $\overline{B_{base,i}}$. This $\overline{B_{base,i}}$ is defined as the beam-averaged backscatter arising from mostly suspended sand, but in combination with the relatively small amounts from fine sediment present.

The first requirement ensures that the *BBC* relation and its parameters describe the acoustic response of the sand suspension only. Therefore, only cases where the fine-sediment concentration is low compared with the sand concentration (e.g., $S < 2$), and thus, the fine-sediment contribution to the backscatter is negligible, are included. The second requirement is related to the precision of the final sand concentration and grain-size estimates, which can be improved by using a precise sand suspension whose acoustic response can be modelled. These calibrations can be found in Section S2.1 in the Supporting Information.

The backscatter B' arising from fine sediments relative to $\overline{B_{\text{base,i}}}$ is the correction of the measured backscatter for the backscatter determined by the *BBC* relation (Topping & Wright, 2016, eq. 66):

$$B' = \overline{B_i} - \overline{B_{\text{base,i}}} = \frac{1}{K_{2,\text{i}}} \log_{10}\left[\left(\frac{f_{\text{sed,i}}}{f_{\text{sand, ref,i}}}\right)^2 \left(\frac{D_{50,\text{ sand, ref}}}{D_{50,\text{ sed}}}\right)\left(\frac{\rho_{\text{sand,ref}}}{\rho_{\text{sed}}}\right)\left(1+\frac{\overline{C_{\text{fines}}}}{\overline{C_{\text{sand, ref}}}}\right)\right], \tag{8}$$

where $K_{2,\text{i}}$ is the empirical slope in the *BBC* relation (Equation 7) and $f_{\text{sed,i}}$ and $f_{\text{sand, ref, i}}$ are the values of the Thorne and Meral (2008) form function calculated over the total and reference sand grain-size distribution, respectively (see Topping & Wright, 2016, pp. 34–38 for a derivation). The grain-size distribution indexed as 'sed' includes the reference sand distribution and the fine-sediment fraction (see Marggraf, 2024 for details).

3.3 | Dual-frequency *RUTS*-based procedure

The second major part of the dual-frequency method consists of combining the two single-frequency sand concentration estimates to establish continuous time series of sand concentration, $\overline{C_{\text{sand, HADCP}}}$, and median grain size, $\overline{D_{50,\text{ sand, HADCP}}}$, averaged over the entire cross-section (Topping & Wright, 2016, Appendix 8). Its principle is the correction of the backscatter of the higher frequency HADCP for grain-size effects, utilizing the theory-based higher influence of grain size on the lower frequency HADCP.

The difference between the two single-frequency sand concentration estimates is used to determine the sand median grain size (Section S2.2 in the Supporting Information). If the two single-frequency concentration estimates are equal, the sand grain size is equal to the reference sand median grain size $\overline{D_{50,\text{sand,ref}}}$ (see Section 3.4 for its definition and estimation). If the concentration $\overline{C_{\text{sand, high}}}$ estimated by the higher frequency HADCP is higher than the concentration $\overline{C_{\text{sand, low}}}$, the median grain size of the suspended sand is finer than the reference sand grain size and vice versa.

Precisely, the determination of the dual-frequency sand concentration and median grain size requires the two single-frequency concentration estimates, the parameters $K_{1,\text{i}}$ and $K_{2,\text{i}}$ of the two *BBC* relations and the properties of the reference sand suspension (notably the reference sand median grain size $\overline{D_{50,\text{ sand, ref}}}$ and geometric standard deviation $\overline{\sigma_{\text{sand, ref}}}$).

These latter properties are used to determine the theoretical acoustic response of the reference sand suspension, the range-independent unit target strength $UTS_{\text{ref,i}}$ of the reference sand for the lower and higher frequency HADCP, respectively (combining eqs. 48–50 in Topping & Wright, 2016):

$$UTS_{\text{ref,i}} = 10\log_{10}\left(f^2_{\text{sand, ref,i}} \frac{3}{16\pi\rho_{\text{sand}} r_0^2 D_{50,\text{ sand, ref}}}\right) + 10\log_{10}\left(2t_{\text{p,i}} c\pi \left(\frac{0.96}{k_i a_{\text{T,i}}}\right)^2\right), \tag{9}$$

where $f_{\text{sand, ref,i}}$ is the form factor for the reference sand grain-size distribution, ρ_{sand} is the sand density, $t_{\text{p,i}}$ is the acoustic ping duration, c is the speed of sound, k_i is the wave number, and $a_{\text{T,i}}$ is the radius of the transducer of the lower and higher frequency HADCP, respectively. This unit target strength of the reference sand suspension is compared with a wide range of sand suspensions possibly occurring in the field. In this study, these possible sand suspensions are described by median grain sizes ranging from 74 to 1500 μ m and the same geometric standard deviation as the reference sand suspension. Their unit target strength *UTS* is calculated similar to the $UTS_{\text{ref,i}}$ but using the form factor and grain-size distribution corresponding to each possible sand suspension.

The relative unit target strength *RUTS* compares the acoustic response of all possible sand suspensions relative to that of the reference sand suspension (Topping & Wright, 2016, eq. 51):

$$RUTS = UTS - UTS_{\text{ref}}. \tag{10}$$

The results of the SFCP are then combined with the *RUTS* relations to determine the logarithm of the mean cross-sectional sand concentration $\overline{C_{\text{sand, HADCP}}}$ (Topping & Wright, 2016, Appendix 8):

$$\log_{10}\left(\overline{C_{\text{sand, HADCP}}}\right) = K_{1,\text{high}} + K_{2,\text{high}}\left(B_{\text{eff, high}} - RUTS_{\text{high}}\right), \tag{11}$$

where $K_{1,\text{high}}$ and $K_{2,\text{high}}$ are the K_1 and K_2 obtained by the *BBC* relation of the higher frequency HADCP and $B_{\text{eff, high}}$ is the effective backscatter measured by the higher frequency HADCP:

$$B_{\text{eff, high}} = \frac{\left(\log_{10}\left(\overline{C_{\text{sand, high}}}\right) - K_{1,\text{high}}\right)}{K_{2,\text{high}}}. \tag{12}$$

The value of the 'experimental' higher frequency *RUTS*, $RUTS_{\text{high}}$, is determined using the *RUTS* relations (Figure 5). To do so, the input into the *RUTS*-procedure, the 'experimental' lower frequency *RUTS* $RUTS_{\text{low}}$ is determined:

$$RUTS_{\text{low}} = B_{1,\text{low}} - B_{2,\text{low}}, \tag{13}$$

where $B_{1,\text{low}}$ is defined as

$$B_{1,\text{low}} = \frac{\left(\log_{10}\left(\overline{C_{\text{sand, low}}}\right) - K_{1,\text{low}}\right)}{K_{2,\text{low}}}, \tag{14}$$

and $B_{2,\text{low}}$ is

$$B_{2,\text{low}} = \frac{\log_{10}\left(\overline{C_{\text{sand, high}}}\right) - K_{1,\text{low}}}{K_{2,\text{low}}}. \tag{15}$$

On the lower frequency *RUTS*–grain size relation, the corresponding grain size is the dual-frequency acoustic sand grain-size

estimate $\overline{D_{50,\,\mathrm{sand,\,HADCP}}}$. In the next step, this procedure is inverted using the higher frequency *RUTS* relation. The above-determined grain size is used to determine the *RUTS* value on the higher frequency relation. This corresponds to the 'experimental' higher frequency $RUTS_{\mathrm{high}}$ required in Equation (11) to determine the dual-frequency sand concentration.

3.4 | Estimation of the reference suspensions

Reference fine-sediment and sand distributions are required in the dual-frequency *RUTS*-based approach to correct the grain-size bias in single-frequency concentration estimates (Topping & Wright, 2016, pp. 27, 43). Those reference suspensions are used to determine the relative unit target strength *RUTS* (Equation 10) and the sampler measurements for the *BBC* equation (Equation 7). They are constant and specific of a study site and describe the suspension in terms of concentration, median grain size and geometric standard deviation of the grain-size distribution. They refer to cross-sectional averages, as throughout the entire method, thereby averaging out spatial gradients.

Determining them as precisely as possible is essential to obtain reliable sand concentration and median grain-size estimates. Therefore, many suspended-sediment measurements under different hydro-sedimentary conditions are necessary. All acoustically estimated fine-sediment and sand suspensions are compared with the reference suspensions (Section S2.2 in the Supporting Information). The reference median grain size characterizes best the average median grain size over the widest possible observed range in sand and fine-sediment concentrations, respectively. The reference sand concentration $\overline{C_{\mathrm{sand,\,ref}}}$ is the concentration corresponding to the determined median reference grain size.

The reference fine-sediment distribution, described by the median grain size, $D_{50,\mathrm{fines,\,ref}}$, and its geometric standard deviation, $\sigma_{\mathrm{fines,\,ref}}$, is determined iteratively in two steps by comparing models and calculations based on measurements to obtain the best possible fit for the two frequencies. The reference sand grain size, $D_{50,\,\mathrm{sand,\,ref}}$, is determined based on the physical samples only (i.e., without an acoustic-theory component) as described above on the selection of the measurements for the *BBC* relation.

The first step to determine the fine-sediment reference suspension utilizes the theoretical relations between the fine-sediment concentration and the attenuation at each frequency. By testing different values of the median grain size and geometric standard deviation, the slope of the theoretical equation (4) is forced to agree as best as possible with the empirical slopes at both frequencies of the least-squares linear regressions on the measurements (Figure 6a,b).

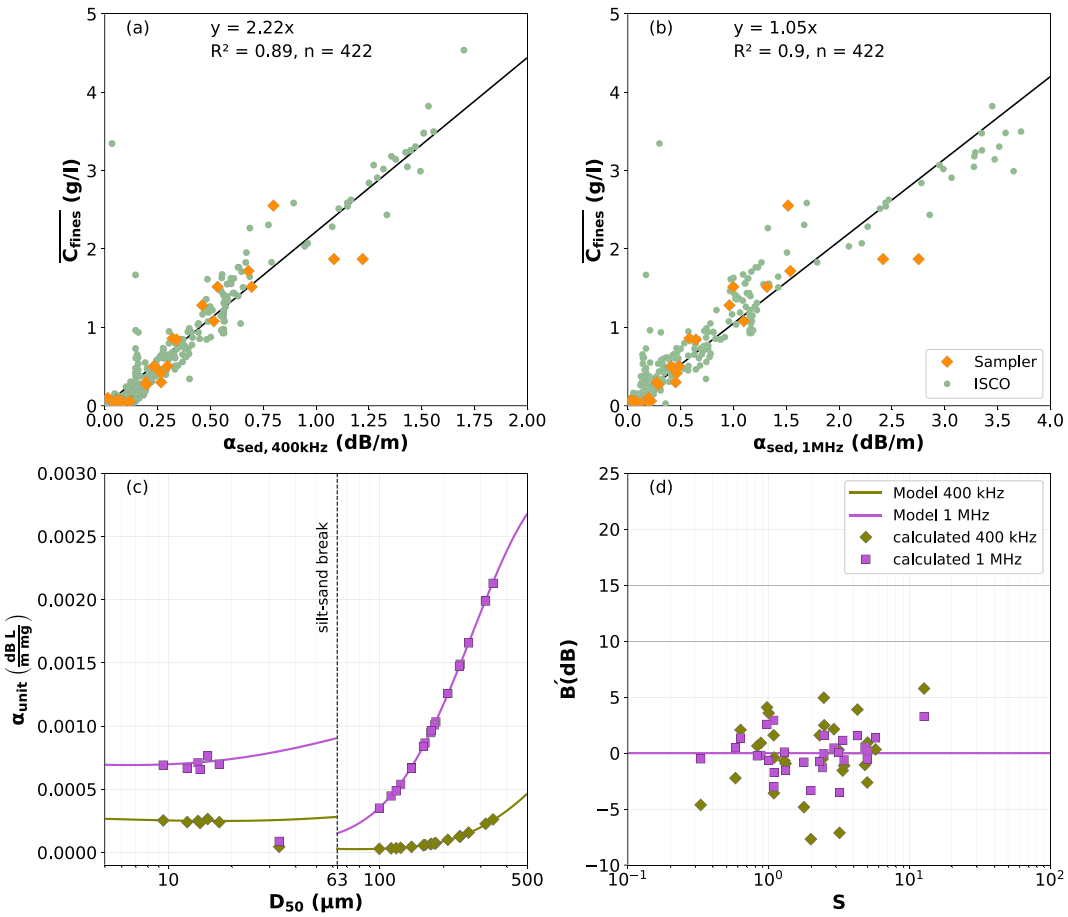

FIGURE 6 Determination and verification of the fine-sediment reference suspension: (a,b) linear regression of the fine-sediment concentration $\overline{C_{\mathrm{fines}}}$ with the attenuation and the sediment-attenuation $\alpha_{\mathrm{sed,\,i}}$ constant for the (a) 400 kHz and (b) 1 MHz HADCP. (c) Modelled (lines) and calculated (symbols) values of the sediment-attenuation constant $\alpha_{\mathrm{unit,\,i}}$ over the occurring fine sediment and sand median grain size D_{50} and (d) modelled (lines) and calculated (symbols) backscatter B_i' to the ratio S of the fine sediment to sand concentration for the 400 kHz and 1 MHz HADCP, respectively. The modelled values of B' at the two frequencies in subfigure d) plot on top of each other at the scale of this plot.

The second step seeks iteratively the best possible agreement between the calculated and modelled values of the B' correction (Equation 8) at both frequencies using the fine-sediment and sand reference median grain sizes and geometric standard deviations (Figure 6). In the River Isère, the modelled B' is near zero at both frequencies over the observed range of S and only becomes important at a fine to sand concentration ratio S of roughly 50 000. Accounting for B' would become much more important with different grain-size distributions.

3.5 | Application variants

Three application variants were evaluated in this study: (1) the original method as proposed by Topping and Wright (2016) and described above, thereafter called TW16; (2) the method TW16-A, a modification of TW16 (Section 3.5.1); and (3) the method TW16-B, a combination of the TW16-A and an index-concentration approach (Section 3.5.2). We developed the two variants TW16-A and TW16-B based on theoretical considerations and local conditions requiring modifications of the original method. The differences between the two variants and the original method are detailed in the following. For all variants, the analysis for a given acoustic measurement is performed only in the far field of the transducer, determined using the Downing critical distance (Downing et al., 1995), and only if at least three valid cells are available to correctly determine attenuation and backscatter.

3.5.1 | Adapted method TW16-A

The general procedure of the TW16-A method is similar to the TW16 method, but several modifications concerning the estimation of the noise floor and the zone of the beam used for analysis were made.

Many acoustic measurements in the River Isère at Grenoble Campus show nonlinear fluid-corrected backscatter profiles, contradicting the hypothesis of homogeneity along the acoustic beam that should lead to linear profiles. In some profiles, backscatter intensities increase with distance or show nonlinear, curved forms (Figure 7). These measurements were mostly made at total sediment concentrations lower than 0.3 g/L and water stages lower than 2.5 m, which corresponds approximately to the sand concentration range ($\overline{C_{sand}} < 0.1$ g/L) with significant deviations between the acoustic estimates and the concurrent measurements (Section S2.3 in the Supporting Information). Most profiles, including the linear ones, measured by both frequencies show a maximum in the fluid-corrected backscatter value within the first metres of the acoustic beam.

To cope with these nonlinear profiles, the zone of the beam included in analysis is adapted to exclude the nonlinear zones of the fluid-corrected backscatter profile. This avoids calculating the slope on a nonlinear profile leading to possibly considerable bias in the acoustic-attenuation estimates.

Instead of applying the user-selected effective-noise floor A_E as in the TW16 method, the TW16-A method uses a two-step approach to determine the cells included into the analysis (see Section S1.2 in the Supporting Information for details). First, a 5 m buffer zone in front of the intersection of the beam and the water surface is applied to exclude possible effects of spurious echoes from the free surface (Nortek, 2018). Second, all cells, where the signal-to-noise ratio SNR is smaller than 1.5 are excluded from the analysis. The last valid cell along the beam was determined as the closest cell to the transducer determined by either the SNR approach or the buffer zone.

Finally, Topping and Wright (2016) typically collect cross-sectional suspended-sediment measurements within less than 30 min using depth-integrating samplers. They use the time-average of the acoustic measurements made within a 1-h window centred on the temporal midpoint of the suspended-sediment measurement in their acoustic calibrations. In contrast, suspended-sediment measurements made using point samplers in this study take up to 4 or 5 h. Therefore, we include all acoustic measurements made during our longer sampling time in the calibrations.

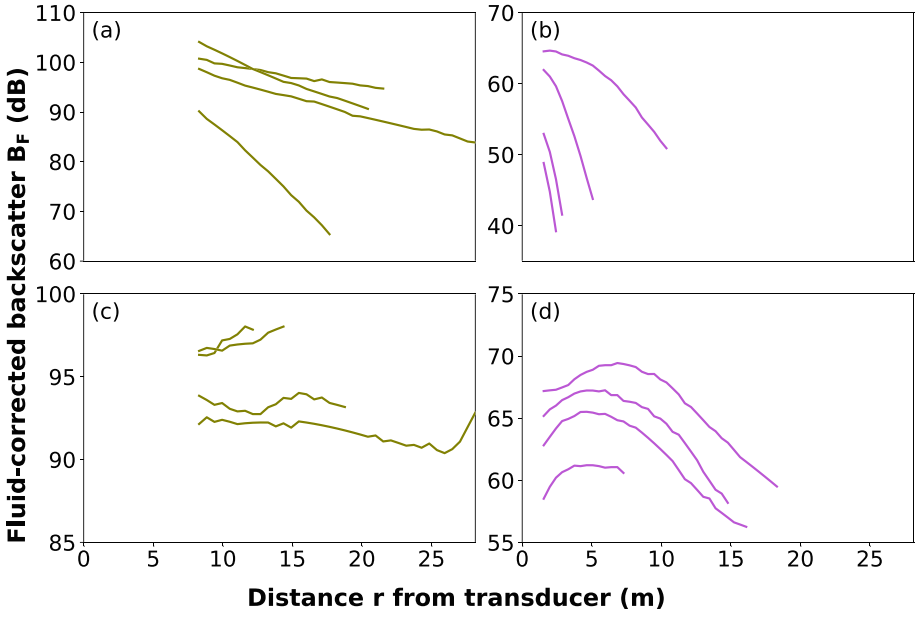

FIGURE 7 Examples of fluid-corrected backscatter profiles measured using the (a,c) 400 kHz and (b,d) 1 MHz HADCPs, showing (a,b) (almost) linear profiles and (c,d) nonlinear profiles at different concentrations ($C_{tot} < 0.3$ g/L) during the study period in the River Isère at Grenoble Campus.

3.5.2 | Modified method TW16-B

The second modified method TW16-B combines the sediment-index-concentration method (Camenen et al., 2023; Santini et al., 2019) and the TW16-A method. In contrast to the TW16 method that relates the acoustic measurements in the ensonified zone to the velocity-weighted concentrations in the entire cross-section (Section 2.2), the TW16-B method introduces an intermediate step following the index-concentration method. First, the acoustic variables are related to the concentrations in the ensonified zone. Then, the concentrations in the ensonified zone are related to the mean cross-sectional concentrations using the relations displayed in Figure 4a,b (Section 2.4). Only the suspended-sediment measurements at the cableway cross-section close to the ensonified zone were included in the analysis.

3.6 | Calibration and evaluation of the three application variants

The calibration of attenuation to the fine-sediment concentration is performed using 422 suspended-sediment measurements made using the US P-6 and US P-72 samplers and the ISCO automatic pump samples covering a fine-sediment concentration range from 0.003 to 4.537 g/L.

The *BBC* calibration relating the beam-averaged backscatter to the concentration of mostly sand (plus minimal amounts of fine sediment) is performed using all sampler suspended-sediment measurements for the TW16 and TW16-A method, whereas only the sampler suspended-sediment measurements in the cableway cross-section collected close to the ensonified zone are used for the TW16-B method. For this study, the conditions preferred by Topping and Wright (2016, p. 31) for the suspended-sediment measurements to be included in the *BBC* relation are extended due to a lack of data (see Section S2.1 in the Supporting Information for the *BBC* relations established for this study). Suspended-sediment measurements were used if the ratios S were smaller than three (instead of $S < 2$), and the sand median grain sizes were within a range of 0.4 ϕ (instead of 0.25 ϕ) centred on the reference sand median grain size (cf. Table 2).

The sand concentration and median grain-size estimates of the three application variants are evaluated in comparison with the concurrent samplings encompassing both the entire cross-section. Based on the uncertainty in acoustic sand concentration and median grain-size predictions (Szupiany et al., 2019; Topping & Wright, 2016), acoustic estimates are considered as acceptably accurate within an error of a factor of two compared with concurrent physical samples.

3.7 | Comparison of acoustic models and measurements

3.7.1 | Relative unit target strength *RUTS*

The modelled relative unit target strength *RUTS* (Equation 10) is compared with the calculated relative unit target strength $RUTS_{calc,\,i}$ to evaluate the performance of the model. The $RUTS_{calc,\,i}$ is calculated for each of the two frequencies and every sampler suspended-sediment measurement using the beam-averaged backscatter $\overline{B_i}$, the logarithm of the sand concentration in mg/L and the parameters of the *BBC* relation:

$$RUTS_{calc,\,i} = \overline{B_i} - (\log(\overline{C_{sand}}) - K_{1,i})/K_{2,i}. \quad (16)$$

3.7.2 | Attenuation and backscatter

To improve the understanding of the acoustic response and explain possible divergences, the modelled and measured attenuation and backscatter are compared following the approaches of Haught et al. (2017) and Vergne et al. (2023). The values of relative backscatter, B_{model}, and attenuation, $\alpha_{sed,\,model}$, are modelled using the suspension properties as in Table 2. They are only calculated for measurements including fine-sediment concentration, that is, the sampler suspended-sediment measurements and corrected ISCO automatic pump samples.

For total suspended-sediment samples, the modelled attenuation $\alpha_{sed,\,model}$ is composed of the attenuation arising from fine sediments $\alpha_{sed,\,fines,\,model}$ and sand-sized sediments $\alpha_{sed,\,sand,\,model}$ (detailed computation in Section S2.4 in the Supporting Information).

For the modelling of the relative backscatter B_{model}, Vergne et al. (2023) use the theoretical determination of the volume backscattering coefficient s_v (Medwin & Clay, 1998) using the instrument calibration constant k_t (Betteridge et al., 2008) (detailed computation in Section S2.4 in the Supporting Information). The value of k_t was not available for the HADCPs deployed in our study. Consequently, the backscatter cannot be modelled easily and the values of k_t ($k_{t,\,400\,kHz} = 3.7 \times 10^6$ and $k_{t,\,1MHz} = 1.8 \times 10^4$) are guessed to obtain a good agreement between modelled and measured values.

4 | RESULTS

4.1 | Dual-frequency *RUTS*-based suspended-sand concentration and grain-size estimates

The agreement between acoustic dual-frequency sand concentration estimates and concurrent measurements varies depending on the application variant and varies within an error of a factor of 2 to 5 (Figure 8). As expected, the acoustic estimates agree better with sampler suspended-sediment data (used for calibration) than with pump PP36 data (used for validation). Most significant underestimations by all three methods occur for low, and therefore unimportant, concentrations.

The sand concentration estimates by the TW16 method are mostly lower than concurrent measurements, and strongly scattered, underestimating high concentrations. A possible reason may be an underestimation of attenuation and backscatter due to the nonlinear fluid-corrected backscatter profiles. The TW16-A method estimates most sand concentrations within an error of a factor of 2 compared with the concurrent samplings. The acoustic estimates are slightly lower than the sand concentrations obtained using the pump PP36 sampler. The TW16-B method yields similar sand concentration

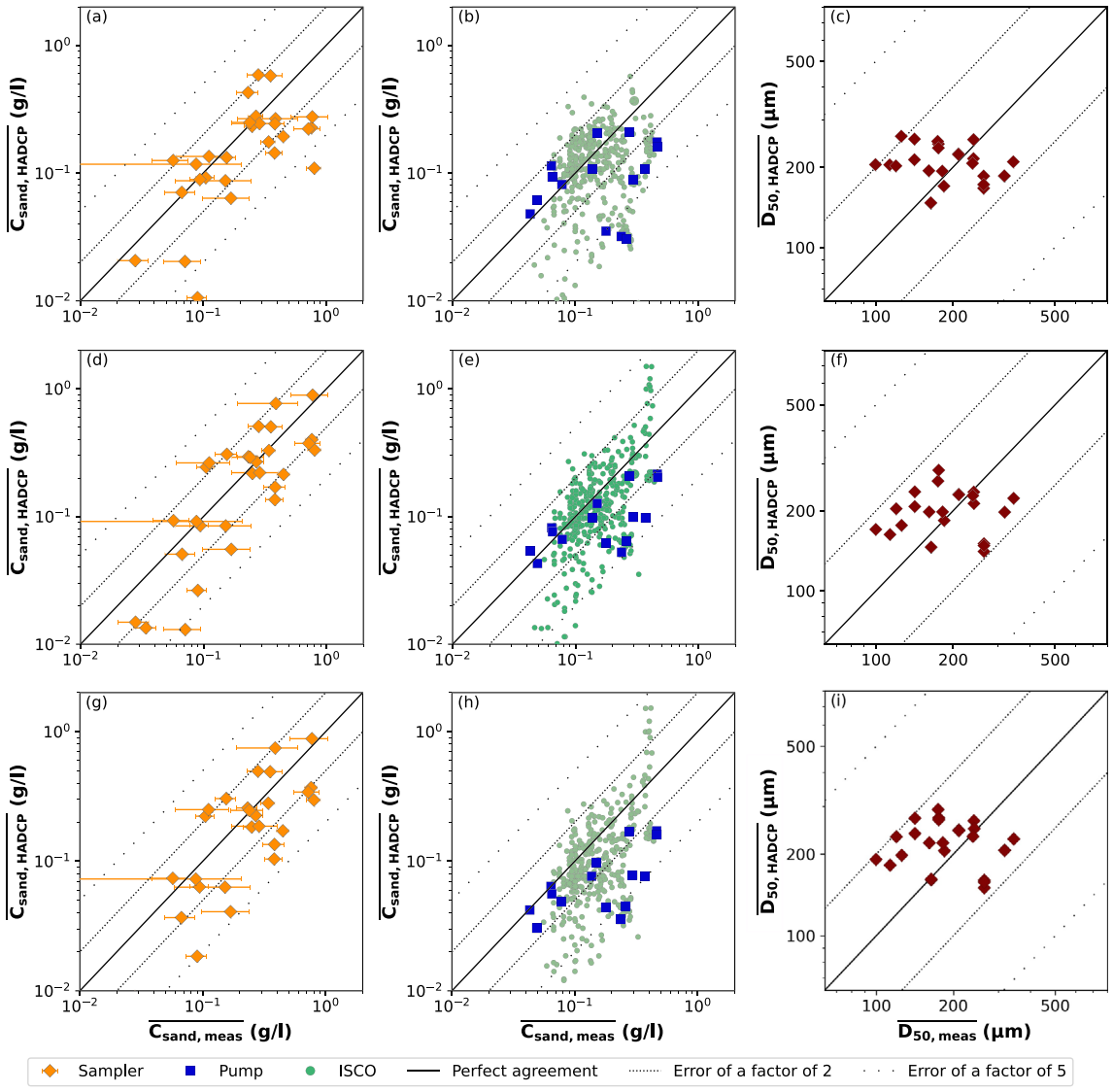

FIGURE 8 Acoustic dual-frequency sand concentration (a,b,d,e,g,h) and sand median grain-size (c,f,i) estimates compared with concurrent suspended-sand measurements of the (a,c,d,f,g,i) calibration data and (b,e,h) validation data consisting of pump PP36 sand concentration measurements and ISCO automatic pump samples during the study period from April 2021 to June 2023 in the River Isère at Grenoble Campus. Acoustic estimates are determined using the (a–c) TW16 method, (d–f) TW16-A method and (g–i) the TW16-B method. The error bars on the sand concentration calibration data (a,d,g) correspond to the uncertainty on the suspended-sand concentration determined by the *SDC* method (Marggraf et al., 2024).

estimates to the TW16-A method, but its estimates are more scattered. The acoustic estimates are systematically lower than the concurrent pump PP36 measurements.

These observed divergences cannot be explained only by the measurement uncertainty in suspended-sand measurements, which was determined following the *SDC* method (Marggraf et al., 2024), but would be rather caused by the acoustic methods themselves, and is consistent with literature (Szupiany et al., 2019; Topping & Wright, 2016).

Ranging within an error of factor of 2 from the line of perfect agreement compared with the median grain-size measurements, the sand median grain-size estimates of the three acoustic methods differ little. Although the acoustic methods estimate the grain size with a higher precision than the sand concentration, they only provide limited additional knowledge compared with the results obtained by physical sampling. For a measured grain size of 200 µ m, the acoustic estimates range between 100 and 400 µ m. This corresponds to an error of a factor of 2 and to the entire measured grain-size range on the calibration dataset.

Finally, among the three application variants, the TW16-A method yields the sand concentration estimates most consistent with concurrent measurements, but like the other acoustic methods, it yields only limited additional knowledge on the grain size.

4.2 | Single-frequency suspended-sand concentration estimates

Similar observations as for the dual-frequency TW16-A method can be made for the TW16-A single-frequency sand concentration estimates. Their results are consistent within an error of a factor of 2 with concurrent measurements, but slightly underestimate the sand concentrations compared with concurrent samplings (Figure 9). The estimates obtained using the TW16-A 400 kHz method are more

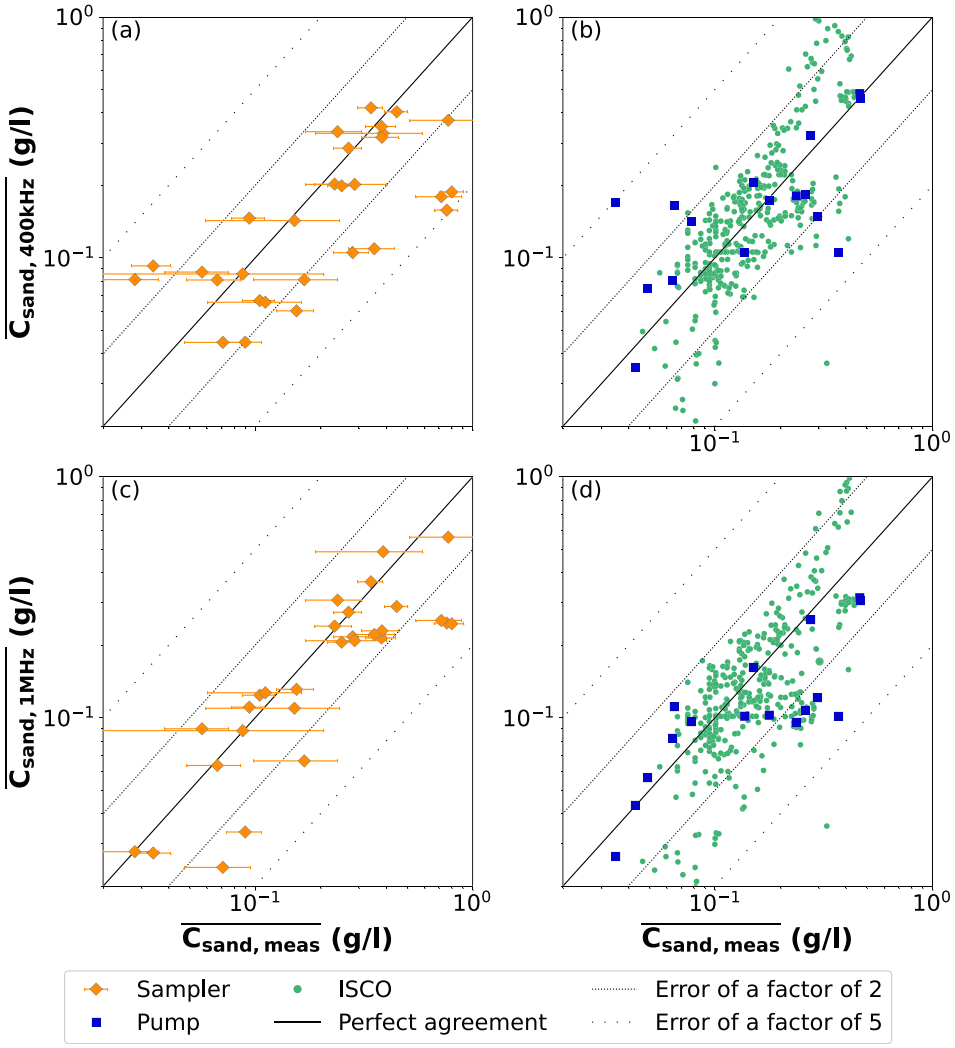

FIGURE 9 Acoustic single-frequency sand concentration estimates compared with concurrent suspended-sand measurements of the (a,c) sampler suspended-sediment measurements used for the calibration and (b,d) pump PP36 sand concentration measurements and ISCO automatic pump samples used for validation during the study period from April 2021 to June 2023 in the River Isère at Grenoble Campus. Acoustic estimates are determined using the TW16-A method. The error bars on the sampler suspended-sediment measurements (a,c) correspond to the uncertainty on the suspended-sand concentration determined by the *SDC* method (Marggraf et al., 2024).

dispersed than the estimates of the TW16-A 1 MHz method. Larger discrepancies between the acoustic and ISCO pump results may be related to the uncertainty in the cross-sectional calibration of the latter, as discussed above. Consequently, higher acoustic concentration estimates are likely more reliable. The single-frequency estimates of the TW16 and TW16-B method are included in Section S3.1 in the Supporting Information.

4.3 | Comparison of different methods estimating the suspended-sand fluxes at Grenoble Campus

The six different methods, the empirical rating curve and five acoustic methods, that is, the three dual-frequency methods (TW16, TW16-A and TW16-B) and two single-frequency methods (TW16-A 400 kHz and TW16-A 1 MHz), estimate total transported sand masses during the study period from April 2021 to June 2023 ranging from 1.35 to 2.59 Mt (Table 4). Over the entire study period, the TW16-A method, the most reliable tested acoustic method and the well-fitted rating curve yield similar total sand masses. Grain-size changes caused by varying sand supply and captured by the dual-frequency acoustic methods apparently average out over multiple years.

These results indicate that the site is located far enough from the sand sources and human river and sand management activities to result in long-term equilibrium processes, for example, by stocking sands in the riverbed or on sand banks. Consequently, the rating-curve method can yield valuable results over longer time periods, which would not be possible at a site strongly influenced by dam operations for example. The TW16-A method, however, likely produces more accurate estimates of sand fluxes during the shorter timescales of individual floods, because it reacts to the changes in sand supply and grain size.

Because all deployed methods are uncertain, the true total sand flux is unknown. Therefore, only relative comparisons can be made, and the most accurate method cannot be identified. Compared with the traditional rating-curve estimates, the relative differences range

TABLE 4 Total suspended-sand fluxes during the study period from April 2021 to June 2023 in the River Isère at Grenoble Campus determined using the described methods.

Method	Total sand mass (Mt)	Relative difference from rating curve (%)
TW16	2.6	24
TW16-A	2.2	5
TW16-B	1.7	−19
TW16-A 400 kHz	1.5	−29
TW16-A 1 MHz	1.3	−38
Rating curve	2.1	-

from −38% to 24%, which is less than a factor of two and thus acceptable. Consequently, these long-term results vary less among the tested methods than the short-term estimates of each method compared with the results of concurrent samplings, where errors of a factor of 2 to 5 are observed.

Analysing the cumulative sand fluxes during the study period shows distinct sensitivities of the tested methods to hydro-sedimentary conditions, particularly at the event scale (Figure 10).

The differences in the total sand masses originate mostly from the spring flood period in 2021. During this period, measured and acoustically estimated sand median grain sizes are finer than the reference sand median grain size, and sand concentrations are higher than the reference sand concentration (see Section S3.2 in the Supporting Information for details; Section 3.4 outlines that reference concentrations and grain sizes are constant for a given study site). All three dual-frequency methods estimate high sand fluxes, whereas the two TW16-A single-frequency methods estimate lower sand fluxes, because they do not consider that the sand was finer than the reference sand. This highlights the biases inherent in the single-frequency methods caused by grain-size changes and the effect of the grain-size correction included in the dual-frequency methods.

The rating-curve method calculates sand transport during low-discharge periods in summer and autumn, whereas the acoustic methods measure hardly any transport. During the snow melt period in spring 2021, the rating-curve method calculates lower sand transport than what the TW16-A method measures, while it estimates higher fluxes in spring 2023 than what the TW16-A method measures. The reason for these discrepancies with opposing signs between the methods is that the sand was finer during the snow melt flood in 2021 than it was in 2023.

Acoustically derived concentrations and grain sizes during a period with high discharges of up to 550 m^3/s in May 2021 illustrate well the general observations (Figure 11). First, the fine-sediment concentrations estimated by the TW16-A method correspond well with the concurrent samplings. Second, the acoustically derived sand concentrations are more variable and differ more from samplings than fine-sediment concentrations. This variability likely indicates both measurement uncertainty and natural fluctuations in time and space in sand concentration, which may account for several orders of magnitude. Although the sand concentration estimated by the single- and

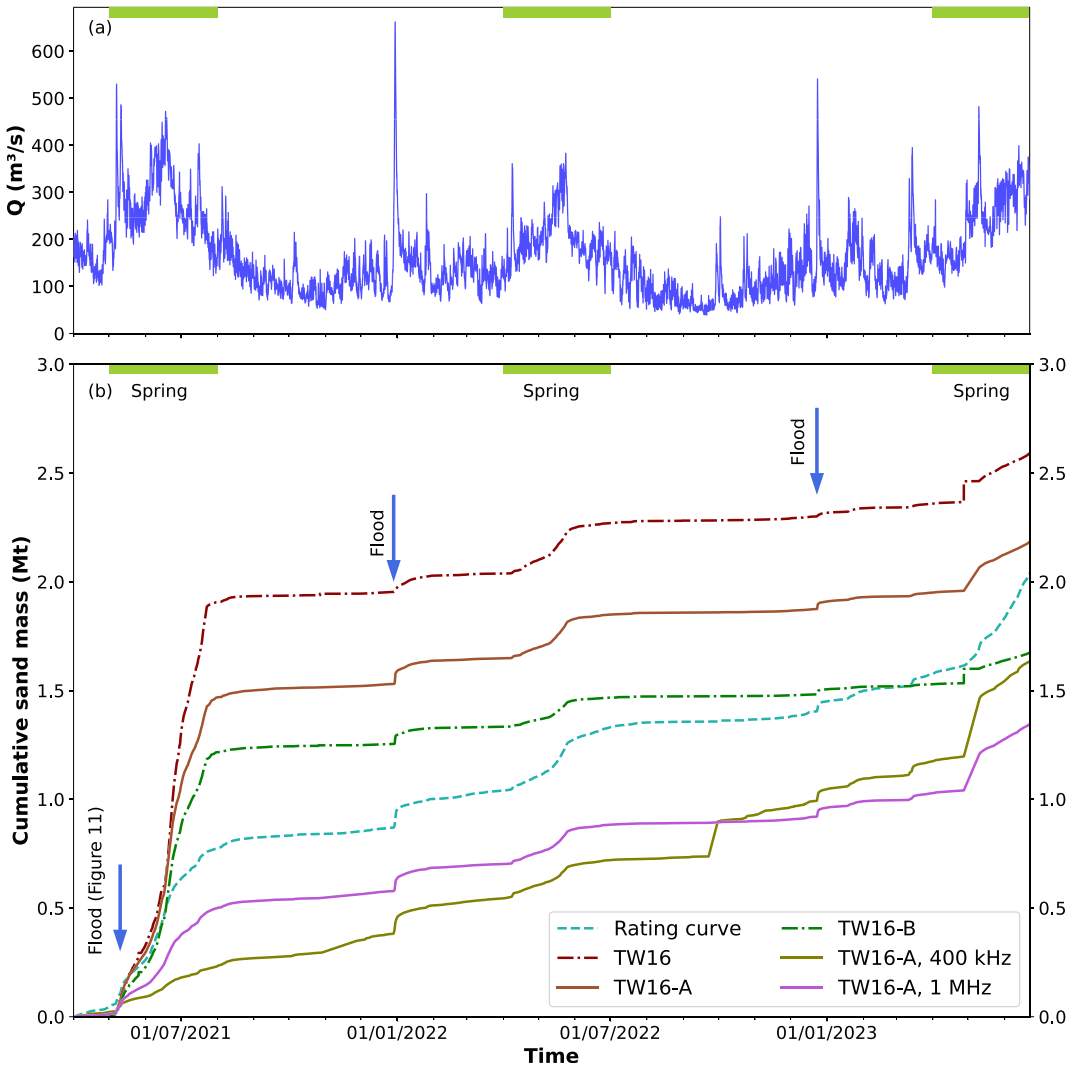

FIGURE 10 Hydro-sedimentary records during the study period from April 2021 to June 2023 in the River Isère at Grenoble Campus: (a) discharge and (b) cumulative sand mass determined using an empirical power rating curve (Equation 1) and five acoustic methods: the TW16, TW16-A and TW16-B method and the two single-frequency parts within the TW16-A method.

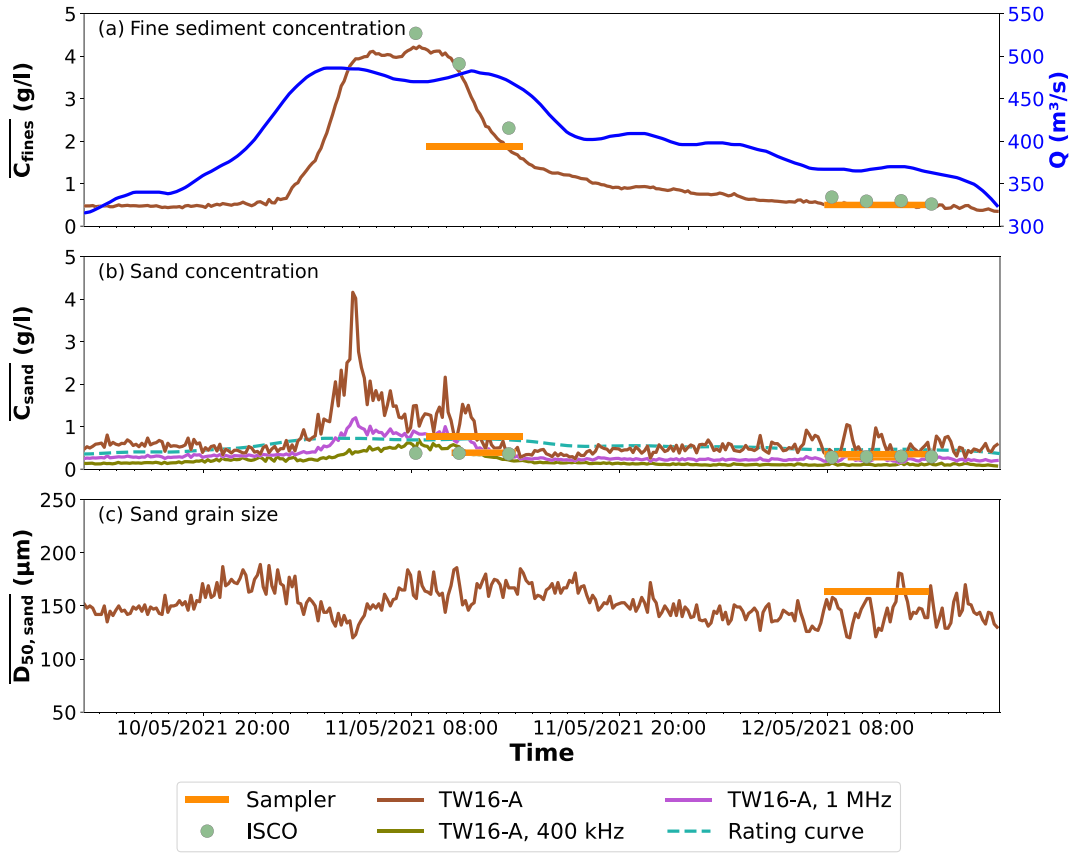

FIGURE 11 Hydro-sedimentary records during a snow melt in May 2021 in the River Isère at Grenoble Campus: (a) discharge and suspended fine-sediment concentration estimated by the TW16-A method and measured by suspended-sediment measurements and ISCO automatic pump samples, (b) suspended-sand concentration estimated by the single- and dual-frequency TW16-A methods and sampler suspended-sediment measurements and calibrated ISCO samples and (c) median sand grain size estimated by the TW16-A method and measured by suspended-sediment measurements.

dual-frequency TW16-A methods strongly fluctuate, the dual-frequency and 1 MHz TW16-A methods estimates are consistent with concurrent samplings. Third, small variations in the sand median grain size are detected by the TW16-A acoustic method. The systematic decrease in grain size during the rising limb of the flood corresponds to that observed in the sampler suspended-sediment measurements (Figure 2d). Because the acoustic dual-frequency method estimates grain-size changes, it can detect at least relative changes in sand median grain size at the event scale.

4.4 | Comparison of acoustic models and measurements

4.4.1 | Relative unit target strength *RUTS*

Considerable scatter in the calculated *RUTS* values occurs for the two frequencies (Figure 12). The slightly higher scatter in the calculated *RUTS* from the 400 kHz HADCP results from the higher scatter about the 400 kHz *BBC* relation. Moreover, a difference between the acoustic models and measurements can be observed which may be caused by a changing relation between the suspended-sediment conditions in the ensonified zone and in the entire cross-section. It may also partially explain the high uncertainties in the sand concentration and grain-size estimations.

4.4.2 | Attenuation and backscatter

For the two frequencies and the US P-6 and US P-72 sampler suspended-sediment measurements and calibrated ISCO pump samples, the modelled and measured attenuation agree acceptably within a factor of 2 (Figure 13a,b). The measurements using the 400 kHz HADCP overestimated the attenuation compared with the model, whereas the 1 MHz measurements slightly underestimated the modelled attenuations. Considerable scatter for attenuations less than ~ 0.1 dB/m, may indicate a lower measurement limit at attenuations of 0.1 dB/m. These results are consistent with previous studies indicating high discrepancies for low attenuations and decreasing discrepancies with increasing concentration (Haught et al., 2017; Topping & Wright, 2016; Vergne et al., 2023). The visible, strong correlations may be explained by the good performance of the used acoustic-attenuation models under the conditions present at the study site and the homogeneity of the suspended fine sediments in the cross-section.

In contrast to the attenuation, modelled and measured backscatter intensities are significantly scattered for the 400 kHz HADCP but agree better for the 1 MHz HADCP (Figure 13c,d). Theoretically, increasing sand concentrations should cause increasing backscatter. Such a trend is clearly visible for the 1 MHz HADCP but not for the 400 kHz HADCP. Similar behaviour is shown by the *BBC* calibrations relating sand concentration to backscatter (Section S2.1 in the

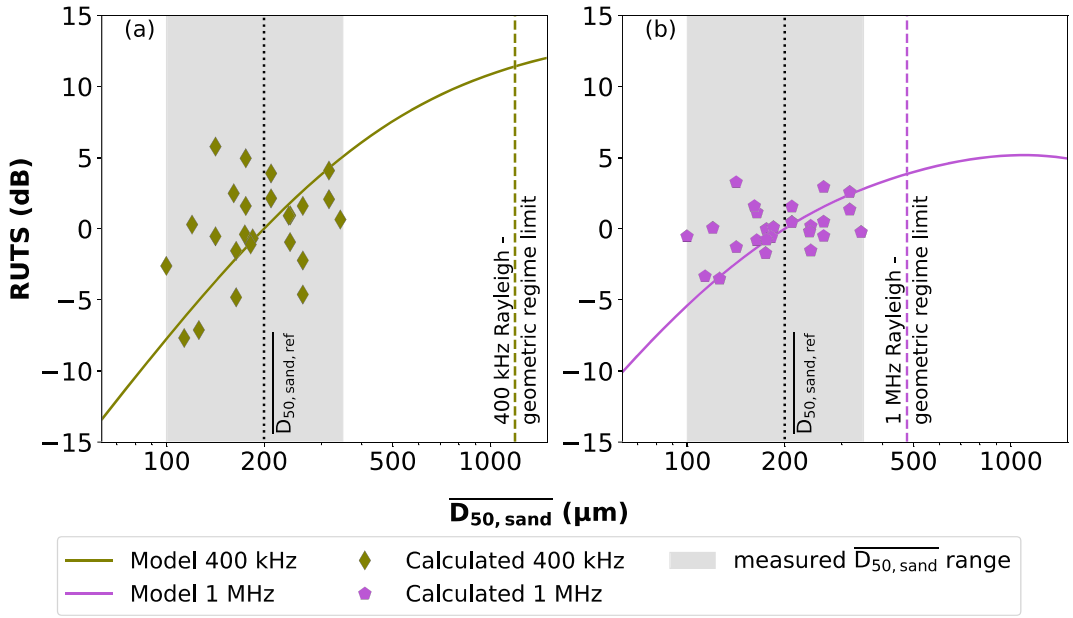

FIGURE 12 Modelled relative unit target strength *RUTS* values (determined in the dual-frequency approach Equation 10) compared with calculated *RUTS* values from the acoustic measurements (Equation 16) made by the (a) 400 kHz and (b) 1 MHz HADCP during the sampler suspended-sediment measurements. *RUTS* values calculated using Equation (12).

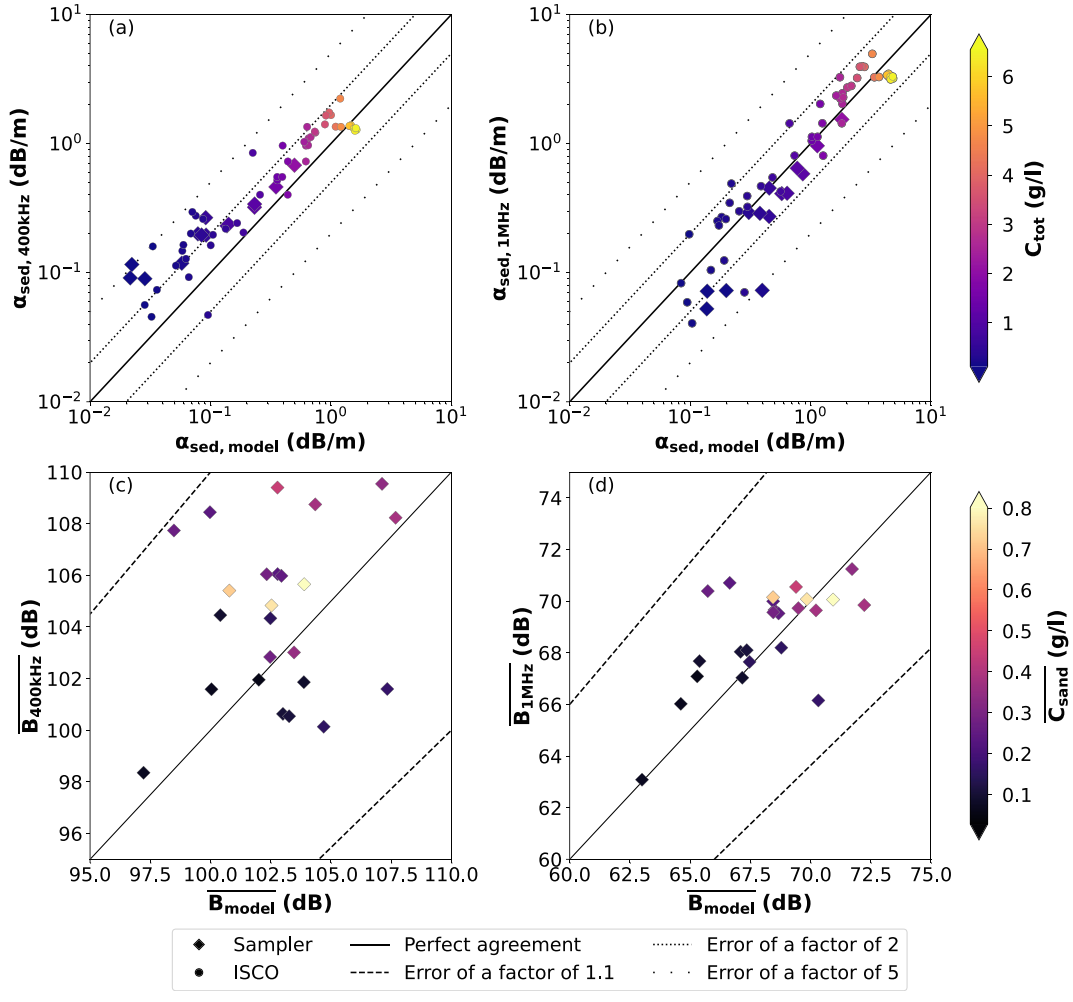

FIGURE 13 Comparison of acoustic parameters determined using the TW16-A method with parameters modelled using (a,b) attenuation $\alpha_{sed, i}$ for the sampler and ISCO datasets and (c,d) backscatter $\overline{B_i}$ for the sampler dataset assuming $k_{t, 400\,kHz} = 3.7 \times 10^6$ and $k_{t, 1MHz} = 1.8 \times 10^4$ for (a,c) the 400 kHz and (b,d) the 1 MHz HADCP.

Supporting Information). Interestingly, the highest sand concentrations do not cause the highest backscatter values at the two frequencies, but the highest backscatter values correspond to moderate sand concentrations. As already stated for the *RUTS* comparisons, the scatter and this final observation both likely arise from variation in how the sediment conditions in the ensonified zone relate to those in the entire cross-section.

5 | DISCUSSION

5.1 | Technical and methodological issues in the applied variants

5.1.1 | Nonlinear fluid-corrected backscatter profiles

Many fluid-corrected backscatter profiles observed in the River Isère at Grenoble Campus increase within the first few metres in the far field or in the distant part of the acoustic beam (Figure 7, see Section S2.3 in the Supporting Information for details). This occurs even after adjusting the zone of the beam used for the analysis for the adapted TW16-A and TW16-B methods (Section S2.3 in the Supporting Information). They do diverge from the expected linear form, required for the determination of the acoustic attenuation. Therefore, it is crucial to pay attention to this issue and adapt the zone of the beam used for analysis, if required, and tested in methods TW16-A and TW16-B.

A possible explanation is that the sediment is not quite homogeneously distributed along the beam (Section S2.4 in the Supporting Information). Another possibility is related to the signal-to-noise ratio, which has been found to influence the signal at signal-to-noise ratios smaller than 10 (Gostiaux & van Haren, 2010). Because almost all our measurements have signal-to-noise ratios smaller than 10, this may explain the nonlinear behaviour in the distant zone of the beam (Haught et al., 2017), but not necessarily in the central part.

Different approaches to cope with nonlinear profiles exist: cutting or correcting nonlinear profiles or profile parts. The two approaches applied in this study are cutting the beam based on specific criteria, either the effective-noise floor, the signal-to-noise ratio or the buffer zone. In contrast, Haught et al. (2017) corrected the initial acoustic signal strength profile by applying a correction proposed by Gostiaux and van Haren (2010). Their approach may be interesting to extend the measurement range under high sediment concentrations when the noise floor is quickly reached. Comparing the Haught et al. (2017) method to the other two approaches using our dataset may improve the correction of nonlinear profiles.

5.1.2 | Data processing when approaching the noise floor

For horizontal ADCPs, the determination of the valid cells along the beam is important, because beam-averaged values are computed and no cell-by-cell analysis is performed as done for vertical deployments. In this study, two different approaches defining the last valid cells were applied: (1) The effective-noise-floor approach for the TW16 method (Topping & Wright, 2016, p. 15 and Appendix 7) and (2) the signal-to-noise ratio approach for the TW16-A and TW16-B methods. In our results, the differences between the two approaches are smaller for the 1 MHz than for the 400 kHz HADCP, for which they depend slightly on the suspended-sediment concentration.

Two reasons question the use of the effective-noise-floor approach as used by Topping and Wright (2016). First, the iterative determination of the most appropriate noise-floor offset for each HADCP is time consuming and user dependent. Second, this method is not able to exclude the nonlinear parts in the distant zone of the 400 kHz fluid-corrected backscatter profiles. In our measurements, the 400 kHz HADCP rarely reaches the noise floor, so that the guess of the noise-floor offset is difficult to impossible.

The signal-to-noise ratio approach applies an objective threshold to separate valid from non-valid data (Vergne et al., 2020). This method is simple, objective and quick.

5.1.3 | Grain-size limit of the *RUTS*-based approach

The dual-frequency approach can only be applied in the Rayleigh regime ($x = ka_s < 1$), because in the geometric regime ($x > 1$), the acoustic response, that is, the form factor, does not depend on the grain size anymore (Hay, 1991; Thorne & Meral, 2008). For the frequencies used in this study, $x = 1$ corresponds to 1194 and 477 μ m for the 400 kHz and the 1 MHz HADCPs, respectively. Though sand-sized flocs are rare in rivers with low organic content particles like the River Isère, the limit between the Rayleigh and geometric regimes in the presence of flocs is reached earlier, because their target strength is higher than the target strength of their primary particles (Fromant et al., 2017; Sahin et al., 2017; Thorne et al., 2014; Vincent & MacDonald, 2015).

Approaching the Rayleigh-geometric regime limit, the *RUTS* curves flatten, which leads to large grain-size variations for small differences in experimental *RUTS*. Consequently, the actual grain size usable for reliable acoustic estimates is much lower than the grain size associated with the regime limit. To avoid this grain-size zone, Dean et al. (2022) recommend to set the upper grain-size limit at the coarsest measured sand grain size. However, this excludes the possibility of coarser grain sizes than those sampled, for example, during specific events or distinct hydro-sedimentary conditions. Fixing such a limit requires stable long-term hydro-sedimentary conditions at the study site and their detailed knowledge and thus a high number of suspended-sediment samplings.

5.2 | Divergences between the acoustic models and measurements

We observe considerable divergences between acoustic models and measurements of attenuation, backscatter and relative unit target strength *RUTS* (Figures 12 and 13). Earlier studies found considerable scatter in attenuation for low concentrations less than 0.1 (Haught et al., 2017) and 1 g/L (Vergne et al., 2023) and better agreement for higher concentrations, as observed for similar frequencies at Grenoble Campus. Frequencies smaller than 0.5 MHz measure attenuations smaller than the modelled results, whereas less differences were

observed using the 1 MHz HADCPs in this study and by Vergne et al. (2023).

Much higher differences occur between the modelled and measured backscatter in this study and in Vergne et al. (2023). We found higher scatter using the 400 kHz HADCP than using the 1 MHz HADCP, in contrast to Vergne et al. (2023) who observed significant dispersion at 1 MHz. However, the k_t values in this study are guessed to obtain optimal agreement, whereas Vergne et al. (2023) have reliable manufacturer information on k_t. Based on theory, the backscatter intensity should increase with concentration, but the backscatter intensities measured using frequencies lower than 500 kHz are affected by large scatter (in this study and Vergne et al., 2023).

The observed divergences between the modelled and measured values may arise from several reasons: (1) the presence of ignored scatterers (not sediment), (2) deviation of the backscatter distribution from the Rayleigh distribution and (3) measurement uncertainties (Vergne et al., 2023).

First, at low concentrations, the influence of clusters of small air bubbles (Shen & Lemmin, 1997) or microstructures (Lavery et al., 2003, 2013; Seim et al., 1995) due to turbulence may become significant due to a lack of particles serving as scatterers (Vergne et al., 2023). As discussed above, flocculation may increase the target strength leading to a quicker transition to the Rayleigh-geometric regime limit (Fromant et al., 2017; MacDonald et al., 2013; Rouhnia et al., 2014; Sahin et al., 2017; Thorne et al., 2014; Vincent & MacDonald, 2015). This effect is supposed to be greater at lower frequencies (Vergne et al., 2023), which may contribute to the divergences between modelled and measured backscatter using the 400 kHz HADCP.

In situ measurements of air bubbles and flocs are essential—but very difficult to obtain—to confirm or discard these assumptions, particularly, if they were available for every suspended-sediment measurement. This may help to correct the acoustic measurements for the observed effects. However, more research is needed to understand the formation of air bubbles and flocs; to evaluate the percentage, structure and density; and to be able to predict their concentration based on hydro-sedimentary conditions, such as flow and wind velocities, particle size or organic matter content.

Second, the deviation of the backscatter distributions from the Rayleigh distributions is considered as another important reason for the observed divergences between acoustic models and measurements (Vergne et al., 2023). It is caused by a very small number of particles of a specific type (Stanton & Clay, 1986; Tuthill et al., 1988) and particularly affects lower frequencies due to their higher sensitivity to large particles, air bubbles and flocs. In this study, large cell sizes were used to decrease this effect (Chu & Stanton, 2010), and the sand concentration was rarely very small compared with the fine-sediment concentration (i.e., large ratios *S*). Therefore, this deviation from Rayleigh statistics may be relatively small.

Third, several measurement uncertainty sources may affect the modelling of the acoustic response, for example, the actual grain-size measurements (Haught et al., 2017; Laible et al., 2023; Vergne et al., 2023), the grain-size integration throughout the cross-section (Marggraf, 2024) and the determination of sand concentration following the *SDC* method (Marggraf et al., 2024). In addition, further uncertainty may be introduced by the comparison of different areas: The measurements were performed along the beam, whereas the modelled values were determined using cross-sectional averages. Due to the spatial heterogeneity of the sand concentration and grain size, its impact may not be negligible. However, this variation along the acoustic beam may cause the nonlinear fluid-corrected backscatter profiles.

Divergences between the modelled and measured *RUTS* may also relate to the calculation of the form factor for fine sediments. The application of commonly used acoustic models may yield major errors, because these models were largely developed for spherical, solid particles, which differ from the actual properties of clay and silt particles (Vergne et al., 2023). Even though the percentage of suspended clays in the suspension in the River Isère at Grenoble Campus is small, the present silt-sized particles are flat and oblate particles with a mica-like structure. These particles may hardly be represented by spherical, solid particles as in acoustic theories used to calculate the form factor.

5.3 | Implications and benefits of this work

A major benefit of this study is the improved explanation and description of the dual-frequency method of Topping and Wright (2016). This clarification of their workflow facilitates the reproducibility of their method. Moreover, the application and adaptation to the River Isère is one of the only studies, where an existing acoustic method has been applied and validated by another research group, enhancing the confidence in this method and its reproducibility. This validation shows the successful estimation of sand (Section 4) and fine-sediment concentration (Section S3.4 in the Supporting Information) and sand median grain size with an error of a factor of 2 under different conditions, coarser sand particles and changing *S* ratios, at the study site of Grenoble Campus.

Another benefit is the enhancement of the Grenoble Campus experimental station by continuous acoustic measurements and the creation of a large open-access dataset composed of acoustic and suspended-sediment sampling data. This hydroacoustic measurement station, initially launched for research purposes, is now continued for the operational monitoring of suspended-sand concentration as the first French hydroacoustic sand-suspension monitoring station. The hourly data acquisition, easy data retrieval and quick acoustic analysis may also allow real-time monitoring of suspended-sand concentration and grain size, for example, under hydro-sedimentary conditions of specific interest, such as floods or dam flushes.

To transpose the dual-frequency approach to another study site, suspended-sediment measurements under all hydro-sedimentary conditions occurring at the study site are required. These samplings may be performed using faster sampling methods that yield mean cross-sectional information such as depth-integrating or pump PP36 sampling to decrease the operational time and costs. In addition to these cross-sectional samplings, one-point samplings on the riverbank may be added. Once calibrated, they offer valuable information on fine-sediment concentrations, as well as sand concentrations when cross-sectional measurements are not possible. Although these samplings represent a non-negligible effort, they are essential for the correct application of this semi-empirical method, for example, to estimate reliable reference suspensions and the *BBC* relations. Even though the grain-size estimation yields limited additional knowledge, using two

frequencies is necessary to obtain reliable sand concentration estimates, due to the correction of the grain-size bias.

6 | CONCLUSIONS

The dual-frequency acoustic method of Topping and Wright (2016) was applied to the River Isère at Grenoble Campus for a study period of 27 months using 400 kHz and 1 MHz HADCPs. Its application required some adaptations to improve the estimations due to local conditions and measured nonlinear profiles. The first adaptation presents the use of the Downing critical distance to apply the method in the acoustic far field only. The second adaptation introduces the use of a buffer zone around the intersection of the acoustic beam with the free surface to avoid spurious echoes. Finally, the iterative and user-dependent estimation of the effective-noise floor was replaced by the quick and objective signal-to-noise ratio approach.

The adapted dual-frequency methods provide acceptably accurate sand concentration estimates at a higher sensitivity to local suspension properties, particularly at the event scale, than a well-fitted empirical rating curve with critical discharge. The dual-frequency results are more accurate than the single-frequency results because they do provide a grain-size correction, whereas single-frequency approaches hardly work in rivers with larger ranges in sand grain size. Concentration and grain-size estimates are affected by less than 100% uncertainty. Compared with sand concentration, acoustic grain-size predictions are more difficult due to the low sand grain-size range. At the event scale, however, the method is sensitive enough to provide additional insights into sand grain-size changes and dynamics.

Considerable differences between modelled and measured relative unit target strength, attenuation and backscatter question the use of the solid-particle theory for cohesive fluvial particles, where further scatterers such as air bubbles and flocs may contribute to the acoustic response.

Finally, this work shows the ability of acoustic methods to estimate and predict suspended-sand concentrations continuously and with uncertainty levels compatible with operational purposes. Monitoring sand grain size proved difficult in the River Isère, even with dual-frequency methods. To overcome this issue, further research may focus on the use of more frequencies and the development of acoustic theories for particles differing from spherical solid particles, such as oblate or flat (clay) particles or flocs.

NOMENCLATURE

Roman symbols

a_s	particle radius (m)
a	equation coefficient in the sediment-rating curve (-)
a_T	radius of the transducer (m)
A	acoustic amplitude (counts)
A_E	effective-noise floor (dB)
A_N	instrument-noise floor (counts)
A_{offset}	noise-floor offset (counts)
b	equation coefficient in the sediment-rating curve (-)
b_{SF}	scalefactor (dB/m)
B	backscatter (dB)
B'	backscatter arising from fine sediments (dB)
$\overline{B}$	beam-averaged backscatter (dB)
$\overline{B_{base}}$	beam-averaged backscatter used to establish the *BBC* relation (dB)
$B_{eff,\,high}$	effective backscatter of the higher frequency HADCP (dB)
B_F	fluid-corrected backscatter (dB)
B_{model}	modelled backscatter (dB)
$B_{1,low}$	first effective backscatter of the lower frequency HADCP (dB)
$B_{2,low}$	second effective backscatter of the lower frequency HADCP (dB)
c	speed of sound (m/s)
$\overline{C_{fines}}$	mean cross-sectional suspended fine-sediment concentration (g/L)
$\overline{C_{fines,\,HADCP}}$	mean cross-sectional suspended fine-sediment concentration estimated by the acoustic method (g/L)
$C_{fines,\,ISCO}$	suspended fine-sediment concentration measured using an ISCO sampler (g/L)
$\overline{C_{sand}}$	mean cross-sectional suspended-sand concentration (g/L)
$C_{sand,\,ISCO}$	suspended-sand concentration measured using an ISCO sampler (g/L)
$C_{sand,\,ISCO,\,corr}$	calibrated suspended-sand concentration measured using an ISCO sampler based on the index concentration method (g/L)
$\overline{C_{sand,\,meas}}$	mean cross-sectional suspended-sand concentration determined by concurrent measurements (g/L)
$\overline{C_{sand,\,ref}}$	mean cross-sectional reference suspended-sand concentration (g/L)
$\overline{C_{sand,\,sampler}}$	mean cross-sectional suspended-sand concentration obtained by sampler suspended-sediment measurements (g/L)
C_{tot}	suspended-sediment concentration obtained by turbidity measurements (g/L)
$\overline{D_{50,\,fines}}$	mean cross-sectional median fine-sediment grain size
$\overline{D_{50,\,sand}}$	mean cross-sectional median sand grain size
$\overline{D_{50,\,sand,\,HADCP}}$	mean cross-sectional median sand grain size estimated by the acoustic method
$\overline{D_{50,\,sand,\,ref}}$	mean cross-sectional median grain size of the reference sand grain-size distribution
$\overline{D_{50,\,sed}}$	mean cross-sectional median sediment grain size
f_∞	form factor (-)
$f_{sand,\,ref}$	value of the Thorne and Meral (2008) form function over the reference sand grain-size distribution (-)
f_{sed}	value of the Thorne and Meral (2008) form function over the total grain-size distribution (-)
k	acoustic wave number (m^{-1})
k_t	instrument calibration constant
K_a	slope of the α_{sed}–C_{fines} relation
$K_{1,low}$	coefficient of the lower frequency HADCP *BBC* relation
$K_{1,high}$	coefficient of the higher frequency HADCP *BBC* relation
$K_{2,low}$	coefficient of the lower frequency HADCP *BBC* relation
$K_{2,high}$	coefficient of the higher frequency HADCP *BBC* relation

Q	multiple-transect average liquid discharge (m^3/s)
Q_{cr}	critical discharge used in empirical sediment rating curve (m^3/s)
UTS	unit target strength (dB)
UTS_{ref}	unit target strength of the reference sand distribution (dB)
r	distance from the transducer (m)
r_0	reference distance of 1 m from the transducer (m)
$RUTS$	relative unit target strength (dB)
$RUTS_{sand,\ ref}$	theoretical $RUTS$ for the reference sand distribution (dB)
s_v	backscattering cross-section of a unit reverberating volume ($1/m^3$)
S	ratio of the mean cross-sectional suspended fine-sediment concentration to the suspended-sand concentration $\overline{C_{fines}}/\overline{C_{sand}}$ (-)
SNR	signal-to-noise ratio (-)
t_p	acoustic ping duration (s)

Greek symbols

α_{sed}	acoustic attenuation related to the sediments (m^{-1})
$\alpha_{sed,\ model}$	modelled acoustic attenuation related to the sediments (m^{-1})
$\alpha_{sed,\ model,\ fines}$	modelled acoustic attenuation related to the fine sediments (m^{-1})
$\alpha_{sed,\ model,\ sand}$	modelled acoustic attenuation related to the sands (m^{-1})
α_{unit}	sediment-attenuation constant (m^{-1})
α_w	coefficient of absorption of acoustic energy in water (dB/m)
ρ_{sand}	density of the sand suspension (kg/m^3)
$\rho_{sand,\ ref}$	density of the reference sand suspension (kg/m^3)
ρ_{sed}	density of the suspended-sediment (kg/m^3)
σ_{fines}	geometric standard deviation of the log-normal fine-sediment grain-size distribution (Φ)
σ_{sand}	geometric standard deviation of the log-normal sand grain-size distribution (Φ)
$\sigma_{sand,\ ref}$	geometric standard deviation of the log-normal grain-size distribution of the reference sand distribution (Φ)
Φ_{rc}	suspended-sand flux determined using the rating curve (kg/s)
Φ_{sand}	suspended-sand flux (kg/s)
ψ	downing near-field correction (-)
ζ	sediment-attenuation constant ((dB L)/(m g))

ACKNOWLEDGEMENTS

The authors thank numerous colleagues for their help with field work and laboratory analysis and Blaise Calmel (INRAE) for his help on data analysis and programming. This study was conducted within the Rhône Sediment Observatory (OSR), a multipartner research program funded through the Plan Rhône by the European Regional Development Fund (ERDF), Agence de l'Eau RMC, CNR, EDF and three regional councils (Auvergne-Rhône-Alpes, PACA and Occitanie). This work has been supported by INRAE, CNR and EDF. Any use of trade, firm or product names is for descriptive purposes only and does not imply endorsement by the US government.

DATA AVAILABILITY STATEMENT

Suspended-sediment measurements and ISCO automatic pump sampler data are available at https://doi.org/10.57745/YTCYSX and described by Marggraf (2024), acoustic data are available at https://doi.org/10.57745/KRY5DX, discharge and turbidity data are available at a public online database called 'Base de Données des Observatoires en Hydrologie (BDOH)' (Thollet et al., 2021) on https://dx.doi.org/10.17180/OBS.ARC-ISERE. The Python codes required for data analysis, acoustic signal inversion and visualization are available on https://github.com/JessicaMarggraf/Acoustic-sand-flux-analysis.

ORCID

Jessica Marggraf https://orcid.org/0000-0002-9372-5494

Guillaume Dramais https://orcid.org/0000-0002-2703-9314

REFERENCES

Aleixo, R., Guerrero, M., Nones, M. & Rüther, N. (2020) Applying ADCPs for long-term monitoring of SSC in rivers. *Water Resources Research*, 56(1), e2019WR026087. Available from: https://doi.org/10.1029/2019WR026087

Antoine, G., Camenen, B., Jodeau, M., Némery, J. & Esteves, M. (2020) Downstream erosion and deposition dynamics of fine suspended sediments due to dam flushing. *Journal of Hydrology*, 585, 124763. Available from: https://doi.org/10.1016/j.jhydrol.2020.124763

Asselman, N.E.M. (2000) Fitting and interpretation of sediment rating curves. *Journal of Hydrology*, 234, 228–248. Available from: https://doi.org/10.1016/S0022-1694(00)00253-5

Betteridge, K.F.E., Thorne, P.D. & Cook, R.D. (2008) Calibrating multi-frequency acoustic backscatter systems for studying near-bed suspended sediment transport processes. *Continental Shelf Research*, 28, 227–235. Available from: https://doi.org/10.1016/j.csr.2007.07.007

Beuselinck, L., Govers, G., Poesen, J., Degraer, G. & Froyen, L. (1998) Grain-size analysis by laser diffractometry: comparison with the sieve-pipette method. *Catena*, 32(3), 193–208. Available from: https://doi.org/10.1016/S0341-8162(98)00051-4

Camenen, B., Dramais, G., Laible, J., Le Coz, J., Pierrefeu, G. & Lauters, F. (2023) Quantification of continuous sand flux time-series downstream of a dam during a flushing event. *Environmental Fluid Mechanics*, 24, 739–755. Available from: https://doi.org/10.1007/s10652-023-09955-9

Camenen, B. & Larson, M. (2008) A general formula for noncohesive suspended sediment transport. *Journal of Coastal Research*, 24(3), 615–627. Available from: https://doi.org/10.2112/06-0694.1

Camenen, B., Le Coz, J., Dramais, G., Peteuil, C., Fretaud, T., Falgon, A. et al. (2014) A simple physically-based model for predicting sand transport dynamics in the Lower Mekong River. In *River flow 2014*, CRC Press: Lausanne; 2189–2197.

Campbell, F.B. & Bauder, H.A. (1940) A rating-curve method for determining silt-discharge of streams. *Eos, Transactions American Geophysical Union*, 21(2), 603–607. Available from: https://doi.org/10.1029/TR021i002p00603

Chu, D. & Stanton, T.K. (2010) Statistics of echoes from a directional sonar beam insonifying finite numbers of single scatterers and patches of scatterers. *IEEE Journal of Oceanic Engineering*, 35(2), 267–277. Available from: https://doi.org/10.1109/JOE.2009.2037988

Cohn, T.A., Delong, L.L., Gilroy, E.J., Hirsch, R.M. & Wells, D.K. (1989) Estimating constituent loads. *Water Resources Research*, 25(5), 937–942. Available from: https://doi.org/10.1029/WR025i005p00937

Darby, S.E., Dunn, F.E., Nicholls, R.J., Rahman, M. & Riddy, L. (2015) A first look at the influence of anthropogenic climate change on the future delivery of fluvial sediment to the Ganges-Brahmaputra-Meghna delta. *Environmental Science: Processes & Impacts*, 17(9), 1587–1600. Available from: https://doi.org/10.1039/C5EM00252D

de Lange, S.I., Sehgal, D., Martínez-Carreras, N., Waldschläger, K., Bense, V., Hissler, C. et al. (2024) The impact of flocculation on in

situ and ex situ particle size measurements by laser diffraction. *Water Resources Research*, 60(1), e2023WR035176. Available from: https://doi.org/10.1029/2023WR035176

Dean, D.J., Topping, D.J., Buscombe, D.D., Groten, J.T., Ziegeweid, J., Fitzpatrick, F.A. et al. (2022) The use of continuous sediment-transport measurements to improve sand-load estimates in a large sand-bedded river: the lower Chippewa River, Wisconsin. *Earth Surface Processes and Landforms*, 47(8), 2006–2023. Available from: https://doi.org/10.1002/esp.5360

Downing, A., Thorne, P.D. & Vincent, C.E. (1995) Backscattering from a suspension in the near field of a piston transducer. *Journal of The Acoustical Society of America*, 97(3), 1614–1620. Available from: https://doi.org/10.1121/1.412100

Dumas, D. (2007) The results of 10 years of daily observations of the flux of suspended matter in one of the main watercourses in the European Alps: the Isere at Grenoble (France). *Comptes Rendus Geoscience*, 339(13), 810–819. Available from: https://doi.org/10.1016/j.crte.2007.09.003

Edwards, T.K. & Glysson, G.D. (1999) Field methods for measurement of fluvial sediment. In *Techniques of Water-Resources Investigations of the U.S. Geological Survey Book 3, Applications of Hydraulics Chapter C2*. Reston, VA, USA: U.S. Geological Service.

FISP. (1941) Study of methods used in measurement and analysis of sediment loads in streams: report n°3: analytical study of methods of sampling suspended sediment, USACE/USGS/USDA/Iowa Institute of Hydraulic Research, Iowa University. Iowa.

Fromant, G., Floc'h, F., Lebourges-Dhaussy, A., Jourdin, F., Perrot, Y., Le Dantec, N. et al. (2017) In situ quantification of the suspended load of estuarine aggregates from multifrequency acoustic inversions. *Journal of Atmospheric and Oceanic Technology*, 34(8), 1625–1643. Available from: https://doi.org/10.1175/JTECH-D-16-0079.1

Gostiaux, L. & van Haren, H. (2010) Extracting meaningful information from uncalibrated backscattered echo intensity data. *Journal of Atmospheric and Oceanic Technology*, 27, 943–949. Available from: https://doi.org/10.1175/2009JTECHO704.1

Grasso, D.A. & Jakob, A. (2003) Charge de sédiments en suspension: comparaison entre deux méthodes de calcul. *GWA*, 83(12), 898–905.

Hanes, D.M. (2012) On the possibility of single-frequency acoustic measurement of sand and clay concentrations in uniform suspensions. *Continental Shelf Research*, 46, 64–66. Available from: https://doi.org/10.1016/j.csr.2011.10.008

Haught, D.W. & Venditti, J.G. (2023) Acoustically-derived sediment-index methods in large rivers: assessment of two acoustic inversion models. *Water Resources Research*, 59(3), e2022WR033278. Available from: https://doi.org/10.1029/2022WR033278

Haught, D., Venditti, J.G. & Wright, S.A. (2017) Calculation of in situ acoustic sediment attenuation using off-the-shelf horizontal ADCPs in low concentration settings. *Water Resources Research*, 53(6), 5017–5037. Available from: https://onlinelibrary.wiley.com/doi/abs/10.1002/2016WR019695

Hay, A.E. (1983) On the acoustic detection of suspended sediment at long wavelengths. *Journal of Geophysical Research*, 88, 7525–7542. Available from: https://doi.org/10.1029/JC088iC12p07525

Hay, A.E. (1991) Sound scattering from a particle-laden, turbulent jet. *The Journal of the Acoustical Society of America*, 90(4), 2055–2074. Available from: https://doi.org/10.1121/1.401633

Hicks, D.M. & Gomez, B. (2016) *Tools in fluvial geomorphology*, 2 In: Kondolf, G. M., Piégay, H. Wiley: Chichester, UK. Available from: https://doi.org/10.1002/9781118648551

ISO 4363. (2002) Measurement of liquid flow in open channels—methods for measurement of characteristics of suspended sediment. Geneva, Switzerland: International Organization for Standardization.

Konert, M. & Vanderberghe, J. (1997) Comparison of laser grain size analysis with pipette and sieve analysis: a solution for the underestimation of the clay fraction. *Sedimentology*, 44, 523–535. Available from: https://doi.org/10.1046/j.1365-3091.1997.d01-38.x

Kun, A., Katona, O., Sipos, G. & Barta, K. (2013) Comparison of pipette and laser diffraction methods in determining the granulometric content of fluvial sediment samples. *Journal of Environmental Geography*, 6(4–5), 49–54. Available from: https://doi.org/10.2478/jengeo-2013-0006

Laible, J., Camenen, B., Le Coz, J., Pierrefeu, G., Mourier, B., Lauters, F. et al. (2023) Comparison of grain size distribution measurements of sand-silt mixtures using laser diffraction systems. *Journal of Soils and Sediments*, 23(5), 2310–2325. Available from: https://doi.org/10.1007/s11368-023-03470-6

Landers, M.N., Straub, T.D., Wood, M.S. & Domanski, M.M. (2016) Sediment acoustic index method for computing continuous suspended-sediment concentrations, U.S. Geological Survey Techniques and Methods, book 3, chapter 5. Available from: https://doi.org/10.3133/tm3C5

Lavery, A.C., Geyer, W.R. & Scully, M.E. (2013) Broadband acoustic quantification of stratified turbulence. *The Journal of the Acoustical Society of America*, 134, 40–54. Available from: https://doi.org/10.1121/1.4807780

Lavery, A.C., Schmitt, R.W. & Stanton, T.K. (2003) High-frequency acoustic scattering from turbulent oceanic microstructure: the importance of density fluctuations. *The Journal of the Acoustical Society of America*, 114, 2685–2698. Available from: https://doi.org/10.1121/1.1614258

Lennermark, M. & Hauet, A. (2022) Developing a post-processing software for ADCP discharge measurement piloted by an international and inter-agency group: a unique, ambitious experience… and one that works! EGU General Assembly 2022, Vienna, Austria, 23–27 May 2022. Available from: https://doi.org/10.5194/egusphere-egu22-9379

MacDonald, I.T., Vincent, C.E., Thorne, P.D. & Moate, B.D. (2013) Acoustic scattering from a suspension of flocculated sediments. *Journal of Geophysical Research: Oceans*, 118(5), 2581–2594. Available from: https://doi.org/10.1002/jgrc.20197

Marggraf, J. (2024) Improving methods for the hydroacoustic monitoring of suspended sand concentration and grain size: application to the Isère River at Grenoble Campus. Ph.D. Thesis, University Claude Bernard Lyon 1, Villeurbanne, France.

Marggraf, J., Dramais, G., Le Coz, J., Calmel, B., Camenen, B., Topping, D.J. et al. (2024) River suspended-sand flux computation with uncertainty estimation, using water samples and high-resolution ADCP measurements. *Earth Surface Dynamics*, 12(6), 1243–1266. Available from: https://doi.org/10.5194/esurf-12-1243-2024

Marrugo-Negrete, J., Rodriguez-Espinosa, P.F., Godwyn-Paulson, P., Paternina-Uribe, R.J., Ibarguen Amud, M.Y., Rosso-Pinto, M. et al. (2023) Detecting mass sediment transport and movement tainted by decades of mining activities in river Quito, Western Colombia. *Journal of Cleaner Production*, 394, 136293. Available from: https://doi.org/10.1016/j.jclepro.2023.136293

Medwin, H. & Clay, C.S. (1998) *Fundamentals of acoustical oceanography*. Academic Press: New York.

Moate, B.D. & Thorne, P.D. (2012) Interpreting acoustic backscatter from suspended sediments of different and mixed mineralogical composition. *Continental Shelf Research*, 46, 67–82. Available from: https://doi.org/10.1016/j.csr.2011.10.007

Moate, B.D., Thorne, P.D. & Cooke, R.D. (2016) Field deployment and evaluation of a prototype autonomous two dimensional acoustic backscatter instrument: the Bedform And Suspended Sediment Imager (BASSI). *Continental Shelf Research*, 112, 78–91. Available from: https://doi.org/10.1016/j.csr.2015.10.017

Moore, S.A., Dramais, G., Dussouillez, P., Le Coz, J., Rennie, C. & Camenen, B. (2013) Acoustic measurements of the spatial distribution of suspended sediment at three sites on the Lower Mekong River. *The Journal of the Acoustical Society of America*, 133, 3227. Available from: https://doi.org/10.1121/1.4805133

Moore, S.A., Le Coz, J., Hurther, D. & Paquier, A. (2012) On the application of horizontal ADCPs to suspended sediment transport surveys in rivers. *Continental Shelf Research*, 46, 50–63. Available from: https://doi.org/10.1016/j.csr.2011.10.013

Moore, S.A., Le Coz, J., Hurther, D. & Paquier, A. (2013) Using multi-frequency acoustic attenuation to monitor grain size and concentration of suspended sediment in rivers. *The Journal of the Acoustical*

Society of America, 133, 1959–1970. Available from: https://doi.org/10.1121/1.4792645

Némery, J., Mano, V., Coynel, A., Etcheber, H., Moatar, F., Meybeck, M. et al. (2013) Carbon and suspended sediment transport in an impounded alpine river (Isère, France). *Hydrological Processes*, 27, 2498–2508. Available from: https://doi.org/10.1002/hyp.9387

Nortek (2018) The comprehensive manual for ADCP's. AWAC, AquaDopp, AquaDopp Deepwater, AquaDopp Profiler, AquaDopp Profiler Z-cell, 2D Horizontal Profiler.

RGE ALTI(R). (2021) Institut National de l'Information Géographique et Forestière. Available from: https://geoservices.ign.fr/rgealti [Accessed 15th May 2021].

Rouhnia, M., Keyvani, A. & Strom, K. (2014) Do changes in the size of mud flocs affect the acoustic backscatter values recorded by a Vector ADV? *Continental Shelf Research*, 84, 84–92. Available from: https://doi.org/10.1016/j.csr.2014.05.015

Sahin, C., Verney, R., Sheremet, A. & Voulgaris, G. (2017) Acoustic backscatter by suspended cohesive sediments: field observations, Seine Estuary, France. *Continental Shelf Research*, 134, 39–51. Available from: https://doi.org/10.1016/j.csr.2017.01.003

Santini, W., Camenen, B., Le Coz, J., Vauchel, P., Guyot, J.L., Lavado, W. et al. (2019) An index concentration method for suspended load monitoring in large rivers of the Amazonian foreland. *Earth Surface Dynamics*, 31(3), 654–667. Available from: https://doi.org/10.1002/hyp.11059

Schleiss, A., Cesare, G.D. & Althaus, J.J. (2010) Verlandung der Stauseen gefährdet die nachhaltige Nutzung der Wasserkraft. *Wasser Energie Luft*, 102(1), 31–40.

Schleiss, A., Franca, M., Juez, C. & De Cesare, G. (2016) Reservoir sedimentation. *Journal of Hydraulic Research*, 54(6), 595–614. Available from: https://doi.org/10.1080/00221686.2016.1225320

Schulkin, M. & Marsh, H.W. (1962) Sound absorption in sea water. *The Journal of the Acoustical Society of America*, 34(6), 864–865. Available from: https://doi.org/10.1121/1.1918213

Seim, H.E., Gregg, M.C. & Miyamoto, R.T. (1995) Acoustic backscatter from turbulent microstructure. *Journal of Atmospheric and Oceanic Technology*, 12, 367–380. Available from: https://doi.org/10.1175/1520-0426(1995)012<0367:ABFTM>2.0.CO;2

Shen, C. & Lemmin, U. (1997) Ultrasonic scattering in highly turbulent clear water flow. *Ultrasonics*, 35, 57–64. Available from: https://doi.org/10.1016/S0041-624X(96)00091-1

Stanton, T. & Clay, C. (1986) Sonar echo statistics as a remote-sensing tool: volume and seafloor. *IEEE Journal of Oceanic Engineering*, 11(1), 79–96. Available from: https://doi.org/10.1109/JOE.1986.1145139

Szupiany, R.N., Lopez-Weibel, C., Guerrero, M., Latosinski, F., Wood, M., Dominguez-Ruben, L. et al. (2019) Estimating sand concentrations using ADCP-based acoustic inversion in a large fluvial system characterized by bi-modal suspended-sediment distributions. *Earth Surface Processes and Landforms*, 44(6), 1295–1308. Available from: https://doi.org/10.1002/esp.4572

Thollet, F., Rousseau, C., Camenen, B., Boubkraoui, S., Branger, F., Lauters, F. et al. (2021) Long term high frequency sediment observatory in an alpine catchment: the Arc-Isère rivers, France. *Hydrological Processes*, 35(2), e14044. Available from: https://doi.org/10.1002/hyp.14044

Thorne, P.D. & Hardcastle, P.J. (1997) Acoustic measurements of suspended sediments in turbulent currents and comparison with in-situ samples. *Journal of the Acoustical Society of America*, 101, 2603–2614. Available from: https://doi.org/10.1121/1.418501

Thorne, P.D., Hardcastle, P.J. & Soulsby, R.L. (1993) Analysis of acoustic measurements of suspended sediments. *Journal of Geophysical Research*, 98(C1), 899–910. Available from: https://doi.org/10.1029/92JC01855

Thorne, P.D. & Hurther, D. (2014) An overview on the use of backscattered sound for measuring suspended particle size and concentration profiles in non-cohesive inorganic sediment transport studies. *Continental Shelf Research*, 73, 97–118. Available from: https://doi.org/10.1016/j.csr.2013.10.017

Thorne, P.D., MacDonald, I.T. & Vincent, C.E. (2014) Modelling acoustic scattering by suspended flocculating sediments. *Continental Shelf Research*, 88, 81–91. Available from: https://doi.org/10.1016/j.csr.2014.07.003

Thorne, P.D. & Meral, R. (2008) Formulations for the scattering properties of suspended sandy sediments for use in the application of acoustics to sediment transport processes. *Continental Shelf Research*, 28(2), 309–317. Available from: https://doi.org/10.1016/j.csr.2007.08.002

Topping, D.J., Grams, P.E., Griffiths, R.E., Dean, D.J., Wright, S.A. & Unema, J.A. (2021) Self-limitation of sand storage in a bedrock-canyon river arising from the interaction of flow and grain size. *Journal of Geophysical Research: Earth Surface*, 126(5), e2020JF005565. Available from: https://doi.org/10.1029/2020JF005565

Topping, D.J. & Wright, S.A. (2016) Long-term continuous acoustical suspended-sediment measurements in rivers—theory, application, bias, and error. In 1823, U.S. Geological Survey. Reston, VA Available from: https://doi.org/10.3133/pp1823

Tuthill, T.A., Sperry, R.H. & Parker, K.J. (1988) Deviations from Rayleigh statistics in ultrasonic speckle. *Ultrasonic Imaging*, 10(2), 81–89. Available from: https://doi.org/10.1177/016173468801000201

Urick, R.J. (1948) The absorption of sound in suspensions of irregular particles. *Journal of the Acoustical Society of America*, 20, 283–289. Available from: https://doi.org/10.1121/1.1906373

van Rijn, L. C. (1984) Sediment transport, part II: suspended load transport. *Journal of Hydraulic Engineering*, 110(11), 1613–1641. Available from: https://doi.org/10.1061/(ASCE)0733-9429(1984)110:11(1613)

Venditti, J.G., Church, M., Attard, M.E. & Haught, D. (2016) Use of ADCPs for suspended sediment transport monitoring: an empirical approach. *Water Resources Research*, 52(4), 2715–2736. Available from: https://doi.org/10.1002/2015WR017348

Vergne, A., Le Coz, J. & Berni, C. (2023) Some backscatter modeling issues complicating the sonar-based monitoring of suspended sediments in rivers. *Water Resources Research*, 59(6), e2022WR032341. Available from: https://doi.org/10.1029/2022WR032341

Vergne, A., Le Coz, J., Berni, C. & Pierrefeu, G. (2020) Using a down-looking multifrequency ABS for measuring suspended sediments in rivers. *Water Resources Research*, 56(2), e2019WR024877. Available from: https://doi.org/10.1029/2019WR024877

Vincent, C.E. & MacDonald, I.T. (2015) A flocculi model for the acoustic scattering from flocs. *Continental Shelf Research*, 104, 15–24. Available from: https://doi.org/10.1016/j.csr.2015.05.002

Walling, D. (1977) Limitations of the rating curve technique for estimating suspended sediment loads, with particular reference to British rivers. *Erosion and solid matter transport in inland waters*, 122, 34–78.

Wisser, D., Frolking, S., Hagen, S. & Bierkens, M. F.P. (2013) Beyond peak reservoir storage? A global estimate of declining water storage capacity in large reservoirs. *Water Resources Research*, 49(9), 5732–5739. Available from: https://doi.org/10.1002/wrcr.20452

Wood, M.S., Szupiany, R., Boldt, J., Straub, T. & Domanski, M. (2019) Measuring suspended sediment in sand-bedded rivers using down-looking acoustic Doppler current profilers, Proceedings of the Joint Federal Interagency Sedimentation and Hydrologic Modeling Conference. SEDHYD, Inc.: Reno, Nevada.

SUPPORTING INFORMATION

Additional supporting information can be found online in the Supporting Information section at the end of this article.

How to cite this article: Marggraf, J., Le Coz, J., Camenen, B., Lauters, F., Dramais, G., Pierrefeu, G. et al. (2025) Improving hydroacoustic methods for monitoring suspended-sand flux and grain size in sediment-laden rivers. *Earth Surface Processes and Landforms*, 50(1), e6056. Available from: https://doi.org/10.1002/esp.6056